

Università degli Studi di Padova  
Dipartimento di Fisica e Astronomia  
Corso di Laurea Magistrale in Fisica

---

SCANNING PROBE MICROSCOPY  
OF  
GRAPHENE  
AND SELF-ASSEMBLED MOLECULES

---

Nicola Galvanetto

*ANNO ACCADEMICO 2013/2014*

*Relatore:* Prof. Giampaolo Mistura

*Correlatore:* Prof. Chris Van Haesendonck





# Contents

<b>Introduction</b>	<b>1</b>
<b>1. Graphene</b>	<b>5</b>
1.1. Crystallographic structure . . . . .	6
1.2. Electronic structure and properties . . . . .	7
1.3. Fabrication of graphene . . . . .	12
1.4. Tuning graphene's electronic properties . . . . .	15
<b>2. Introduction to Scanning Probe Microscopy</b>	<b>21</b>
2.1. Scanning Tunnel Microscopy . . . . .	23
2.2. Atomic Force Microscopy . . . . .	25
2.3. Experimental setups . . . . .	27
<b>3. Sample production and characterization</b>	<b>31</b>
3.1. Au films on mica . . . . .	31
3.2. Graphene growth and transfer . . . . .	33
3.3. Graphene on SiO <sub>2</sub> . . . . .	39
3.4. Graphene on Au(111) . . . . .	41
<b>4. Molecules physisorption</b>	<b>49</b>
4.1. DBA-OC <sub>4</sub> . . . . .	49
4.2. DBA-OC <sub>4</sub> on Au(111) . . . . .	50
4.3. DBA-OC <sub>4</sub> on HOPG . . . . .	51
<b>5. Conclusions and Outlooks</b>	<b>55</b>
<b>Acknowledgments</b>	<b>57</b>
<b>A. Tight-binding method for graphene</b>	<b>59</b>
<b>Bibliography</b>	<b>63</b>





# Introduction

The XXI century will be the era of the nano-world. At least scientists are working on it. Starting from Industrial Revolution humans started to build machines to make their life easier and more comfortable but in this mad race they forgot that we live in a finite system, the earth. Natural resources are not inexhaustible: forests can finish, lands can finish, clean water and clean air can finish. In the XV century humans realized that the earth was a sphere, but only in the late XX century we realized that a sphere has a finite surface area and volume, and we should take care of it.



We cannot continue to waste so many resources, but at the same time we are not willing to give up all the comforts we are addicted to. So, what can we do? The idea is to better use the finite resources we have. But, how to do that? Just by discovering a way to let machines do the same work but more efficiently.

The word *nanotechnology* began to become popular in the 1980's when Eric Drexler started to think about building machines on the scale of molecules, a few nanometers size-motors (Fig. 0.1), robot arms, and even whole computers, far smaller than a cell. Drexler spent the next ten years describing and analyzing these incredible devices, and responding to accusations of science fiction. With time nanotechnology became an accepted concept, and its meaning shifted to encompass the simpler kinds of nanometer-scale technology. Thanks to numerical methods it is theoretically possible to simulate and predict atoms behavior at the nano scale. However, building the simulated structures is quite a bit more difficult. Gerd Binnig and Heinrich Rohrer in 1981 invented the scanning tunneling microscope which is actually the most plausible attempt to do that. An STM microscope can be used to

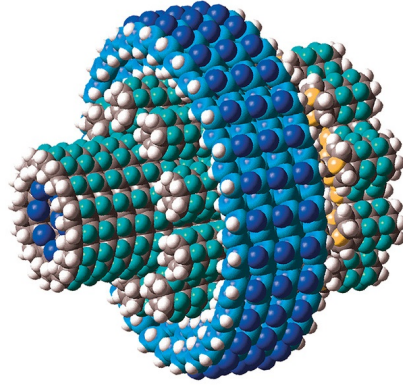


**Figure 0.1.:** With 3432 atoms, this rotor is one of the largest nano-mechanical devices ever modeled in atomic detail.

manipulate atoms, but first of all it is a microscope because you need to know how matter is at that scale before playing with it. But STM manipulations are too slow and are too complex to imagine factories with a million of STM building millions of nano-objects. For mass production different processes must be used.

*“The XXI century will be the era of the nano-world”* maybe is an optimistic prediction, what we can say without any doubt is that the beginning of the XXI century is becoming the era of *graphene* (Fig.0.2). Graphene is the name given to a two dimensional structure of carbon atoms seen for the first time in 2004. Everything revolves around the fact that it is two dimensional, 2D in a 3D world. 2D is a limit, the limit for the nanoscale, and with graphene this limit is not so difficult to be reached. For graphene there are processes that allow its mass production, thus mass production of a nano-structured object. The target seems to be closer. There are hundreds of applications in which graphene is involved, thousands of research groups are working on it and million dollars are spent on studying it.

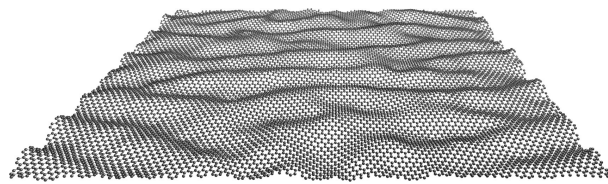


**Figure 0.2.:** Molecular model of the honeycomb lattice of graphene.

We are physicists, we would prefer to combine these interesting applications also with fundamental science. 2D means a lot for physics, 2D means that along the missing dimension the size of our object is the size of atoms, so quantum behavior is directly involved in the physics of this graphene. Now we have an experimental lab for something that before 2004 could only be imagined.

This master thesis focuses on two parallel aspects: the production of graphene and

networks of self-assembled molecules and the scanning probe microscopy techniques which is necessary to investigate them. The thesis is part of a bigger research topic which has the general aim to tune graphene's electronic properties using self-assembled molecules attached to it in order to control electronic bands and in particular open a band gap. The application is directly connected with transistors, the idea is to replace silicon and MOS-FET by using tuned graphene in different transistor's architectures.

The thesis is organized as follows. In the first chapter graphene, its electronic properties and doping processes are discussed. We present a theoretical introduction, then fabrication methods are discussed. In the last section we put more emphasis on different ways to tune the electronic properties, in particular with physisorbed molecules. The second chapter deals with scanning probes techniques. After a detailed description of STM and AFM technologies, the setups used in this work are presented. In the third chapter we discuss the sample preparation and their characterization, including the detailed scanning tunneling microscopy of graphene transferred on gold. In the fourth chapter the experimental work with molecules is discussed. Chapter five presents conclusions and outlooks of this work.



# 1. Graphene

Scientists believed that two dimensional crystals couldn't exist. The reason of their belief is based on thermodynamical observations: a bidimensional structure tends to reduce its surface energy clustering in more stable 3D structure [?] like fullerenes (discovered in 1985) and carbon nanotubes (1991). The first steps for the isolation of a single layer of graphene from graphite were made a long time ago, around the half of the nineteenth century.

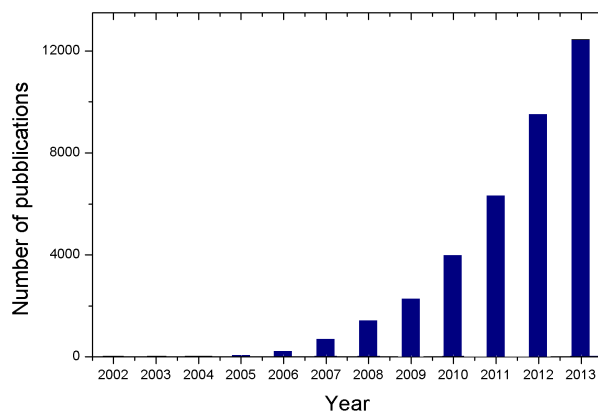


**Figure 1.1.:** Articles with “Graphene” in the title per year. Data provided by Google Scholar.

In 1840 Schafhaeult intercalated potassium in graphite, which means that he was the first to put a chemical species between its layers, and 20 years later Benjamin Collins Brodie discovered the highly lamellar structure of thermally reduced graphite oxide. After that we have to wait until 1947 when a Canadian theoretical physicist, P. R. Wallace, developed the first electronic theory of a layer of graphite [48], which is graphene, showing its uncommon bands structure. But the bigger step to graphene discovery was made by Ulrich Hofman and Hanns-Peter Boehm in 1962 when they looked for the thinnest possible fragments of reduced graphite oxide and identified some of them as monolayers, the Nobel Prize A. K. Geim said. Hence why they were not aware of the Nobel Prize in place of Geim and Novoselov. Geim answer to us:

“I have to mention that the 1962 identification relied on a relative TEM contrast, an approach that would not stand today’s scrutiny because the

contrast strongly depends on focusing conditions. For example, Rahul Nair and I tried but predictably failed to distinguish between monolayers and somewhat thicker flakes by using only their TEM contrast. [...] Nonetheless, the Boehm–Hofmann work should, in my opinion, stand as the first observation of graphene sheets because monolayers should have been present among the residue, and the idea was correct. Furthermore, it was Boehm et al who in 1986 introduced the term *graphene* [17].”

In the 70’s scientists tried a new technique to synthesize graphene in a “*bottom-up*” method: the epitaxial growth, but they didn’t succeed. In the 90’s they tried again from graphite using precision mechanical instrument but they obtained flakes of few hundreds nanometer wide.

In 2004 Andre Geim and Kostantin Novoselov were the firsts to observe monolayer graphene and thanks to this discovery they won the Nobel Prize in 2010 “*for ground-breaking experiments regarding the two-dimensional material graphene*”.

Graphene can be helpful in many fields: in energy storage, as a transparent conducting electrode (touch screen), as a gas sensor for detectors and many others. In particular we focus on microelectronics. Thanks to his high carrier mobility and his unique band structure, experts say that it is a candidate to replace silicon in transistors. First let’s have a look on past and present situation of silicon transistor. In the 60’s Gordon Moore (Intel co-founder) described the trend of integrated circuits in a famous paper entitled “Cramming more components onto integrated circuits” [38]. His conjecture was that the growth of a chip performance increases exponentially in time: it almost doubles in two years. This performance improvement is due to our ability to increase the number of transistor in a chip, so building them smaller. But this process has a physical limit, indeed we cannot manufacture transistor smaller than atoms. As Fig. 1.2 shows, the limit will be probably reached in about ten years. It is clear that this billionaire business needs another technology to survive, and graphene could be the technology they need. The section dedicated to the tuning of electronic properties of graphene will better explain the physics involved in research in this field.

In the first section of this chapter crystallographic structure of graphene is presented. Its uncommon electronic behavior and detail properties is presented in the second section. In the third section it is discussed the methods to manufacture graphene and in the last section is presented an overview on the techniques to tune its electronic properties.

## 1.1. Crystallographic structure

Graphene is a two-dimensional material with a honeycomb lattice with a two-atomic basis as seen in Fig. 1.3. It is truly two-dimensional, which means that only two primitive lattice vectors,  $\mathbf{a}_1$  and  $\mathbf{a}_2$ , are necessary to construct the entire lattice. The length of a carbon-carbon bond in graphene is  $a_0 = 1.42 \text{ \AA}$  and the lattice

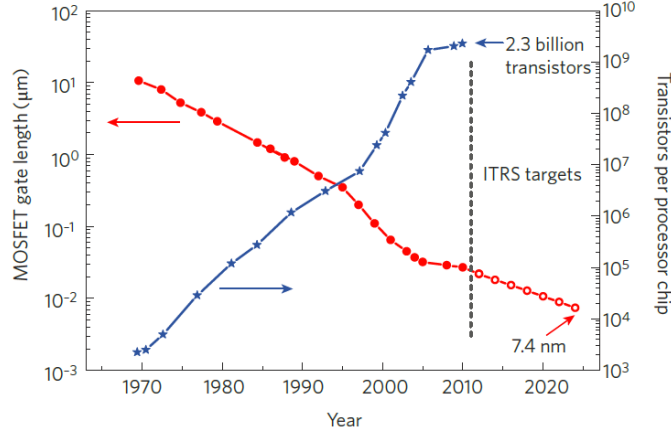


**Figure 1.2.:** [44] Trends in digital electronics. Evolution of MOSFET gate length in production-stage integrated circuits (filled red circles) and International Technology Roadmap for Semiconductors (ITRS) targets (open red circles). As gate lengths have decreased, the number of transistors per processor chip has increased (blue stars).

constant is  $a = 2.46 \text{ \AA}$ . The lattice vectors, describing the position of one atom to the next are:

$$\mathbf{a}_1 = \frac{a}{2} \begin{pmatrix} \sqrt{3} \\ 1 \end{pmatrix}, \quad \mathbf{a}_2 = \frac{a}{2} \begin{pmatrix} \sqrt{3} \\ -1 \end{pmatrix} \quad (1.1)$$

The unit cell of graphene, the smallest unit possible to describe the crystal structure, consists of one atom in A site and another in B shifted of  $\mathbf{a}_0 = a_0 \begin{pmatrix} 1 \\ 0 \end{pmatrix}$ . Fig. 1.3 on the left shows the construction in reciprocal space along with the first Brillouin zone. The reciprocal-lattice vectors are:

$$\mathbf{g}_1 = \frac{2\pi}{\sqrt{3}a} \begin{pmatrix} 1 \\ \sqrt{3} \end{pmatrix}, \quad \mathbf{g}_2 = \frac{2\pi}{\sqrt{3}a} \begin{pmatrix} 1 \\ -\sqrt{3} \end{pmatrix} \quad (1.2)$$

as shown in the figure. Special points in the Brillouin zone are labelled  $\Gamma$ ,  $\mathbf{M}$  e  $\mathbf{K}$  corresponding to the center, edge and corner of the Brillouin zone respectively. The  $\mathbf{K}$  point is of significant importance as it is the location of the Dirac point where all the interesting Physics takes place.

## 1.2. Electronic structure and properties

Despite the simplicity of the hexagonal graphene structure formed by carbon atoms, the electronic behavior shows fascinating and complex properties, giving high expectation for the possible application of graphene in this field. Graphene is formed

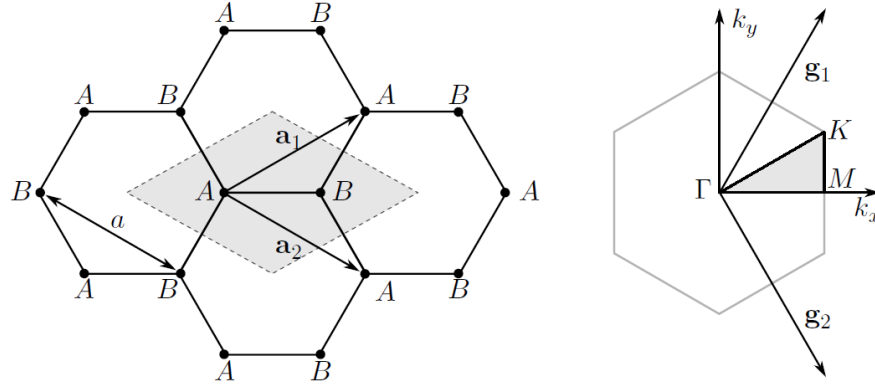


**Figure 1.3.:** Lattice vectors and unit cell (gray) of graphene is shown to the left. Brillouin zone and irreducible Brillouin zone (gray) of graphene is shown to the right. The reciprocal lattice vectors are also shown.

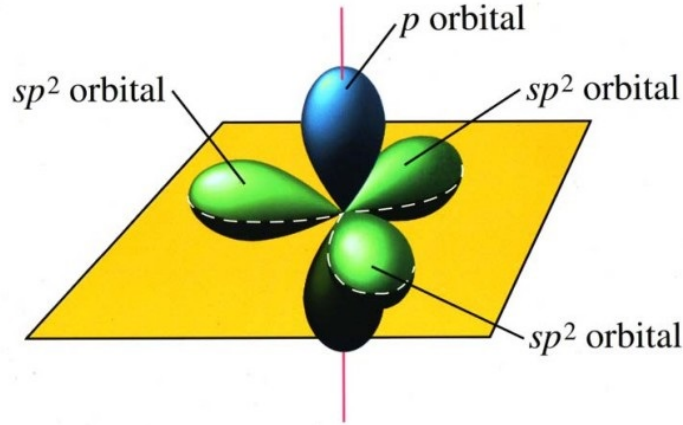


**Figure 1.4.:**  $sp^2$  orbital hybridization of the carbon atoms in graphene.

by a layer of carbon atoms in  $sp^2$  bonding. Fig. 1.4 shows a representative of the orbital comprised of the four valence electrons in each carbon atom when bounded on this  $sp^2$  configuration. It is possible to differentiate the two types of orbital shapes between  $\sigma$  and  $\pi$ .  $\sigma$  bond is form by head-to-head bonding of the planar  $sp^2$  orbitals, yielding a strong covalent bond with the nearest carbon atoms;  $\pi$  represents the  $2p_z$  electron orbital which is perpendicular to the graphene sheet, remains unbounded, and overlaps with the  $\pi$  of its nearest neighbor, giving rise to a particular  $\pi$ -conjugated two-dimensional gases. It is interesting to notice that there is no overlap between  $\pi$  and  $\sigma$  orbitals which gives an advantage for theoretical analysis once each band can be treated independent from the others. By using tight-binding method it is possible to obtain the electronic bands of graphene. Fig. 1.5 shows the electronic band structure of graphene. For simplicity, the Fermi energy is set as zero. Except for the  $\pi$  band, the other bands shows a very large separation between the valence and conduction bands. For the  $\sigma$  bands the shortest gap is more than 10



eV around the  $\Gamma$  point which reveals the strong  $sp^2$  covalent bonding. On the other hand, the  $\pi$  band shows the largest separation at the  $\Gamma$  point, but at the K point the valence and conduction band touch. There is no overlap between  $\pi$  and  $\pi^*$  bands, but there is also not gap in between. Because of that this material is described as semiconductor with zero band gap. Due to this behavior compared with the large gap of the  $\sigma$  bands, the  $\pi$  is the responsible for the particular electronics behavior of graphene. As mentioned before, there is no overlap between the  $\pi$  and  $\sigma$  orbital, simplifying the theoretical analysis allowing the study of the  $\pi$  band independent from the others. Assuming that the electrical behavior of graphene relays on the  $\pi$

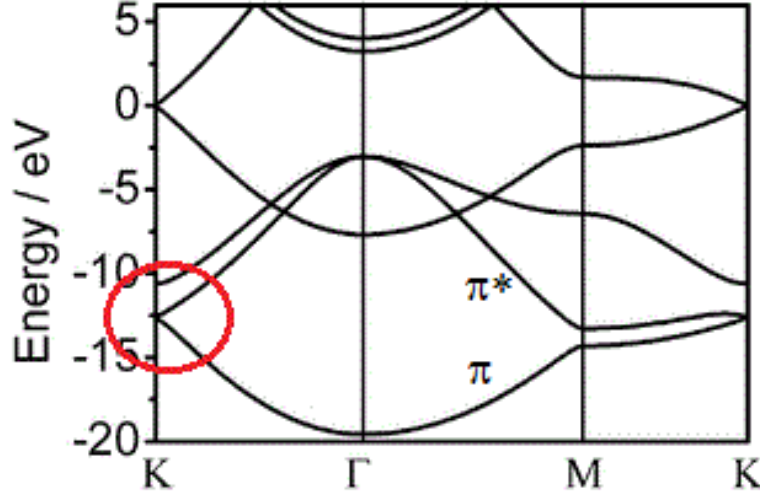


**Figure 1.5.:** Electronic band structure of graphene. In the circle the zero gap between  $\pi$  and  $\pi^*$  bands.

band, by using two adjacent carbon atoms as a unit cell as proposed by Wallace [48], one can use tight-binding method within the first nearest neighbor approximation to deduce the energy dispersion relation. As shown in Appendix A the dispersion for  $\pi$  electrons in graphene is

$$E(\mathbf{k}) = \frac{\epsilon_{2p} \mp \gamma \sqrt{f(\mathbf{k})}}{1 \pm s \sqrt{f(\mathbf{k})}} \quad (1.3)$$

with

$$f(\mathbf{k}) = 1 + 4 \cos^2 \left( k_y \frac{a}{2} \right) + 4 \cos \left( k_y \frac{a}{2} \right) \cos \left( k_x \frac{a\sqrt{3}}{2} \right) \quad (1.4)$$

where  $\epsilon_{2p}$  is the energy of an electron in  $p$  orbital (which can be assumed zero),  $\gamma$  is the hopping energy and  $s$  is the overlap integral.

This expression can be very simplify if we only care about low-energy regime ( $\sim 1$  eV). By expanding 1.3 near K point we find a linear relation between  $E$  and the crystal momentum  $\mathbf{q}$  relative to the one in K-point  $\mathbf{q} = \mathbf{k} - \mathbf{k}_K$ :

$$E = \pm \hbar v_F |\mathbf{q}| \quad (1.5)$$

where  $v_F = \frac{\sqrt{3}a\gamma}{2\hbar} \simeq 10^6 \frac{m}{s}$  is the Fermi velocity. This particular relation means that electrons at low energy behave like photons but with different fixed speed ( $v_F \simeq \frac{c}{300}$ ), thus like massless particle [1]. Contrary in a common semiconductor

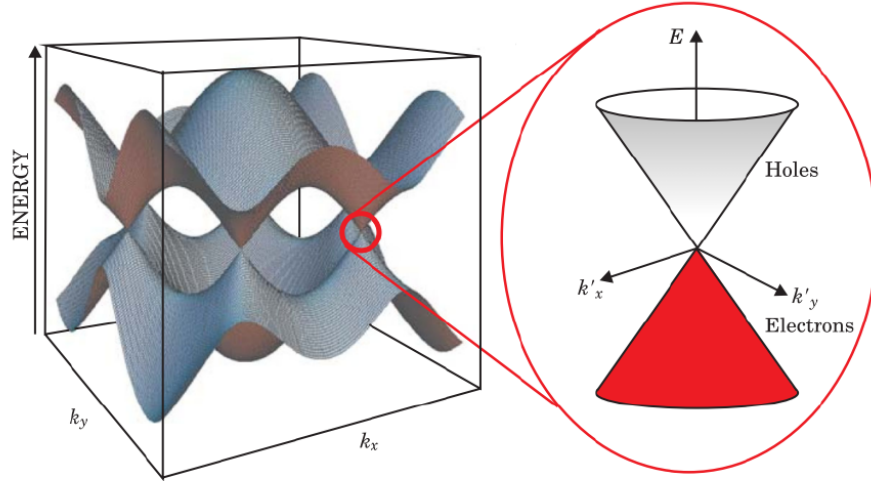


**Figure 1.6.:** Dispersion relation of electrons in graphene with the inset showing the linear bands around the K point.

with parabolic bands electrons energy has the classical quadratic dependence from momentum. This strange electrons behavior in graphene affects also the Density of States, DOS (number of available states to occupy per unit volume and energy). In a conventional 2D semiconductor such as GaAs the DOS is given by  $D(E) = \frac{m}{\pi\hbar^2}$  and is independent of energy, but for graphene near the K point  $E = \hbar v_F |\mathbf{q}|$  instead of  $E = \frac{\hbar^2 k^2}{2m}$  and the DOS becomes:

$$D(E) = \frac{2E}{\pi(\hbar v_F)^2} \quad (1.6)$$

which is linear in energy. Fig. 1.7 shows the DOS for graphene compared to a typical 2D system with parabolic band structure.

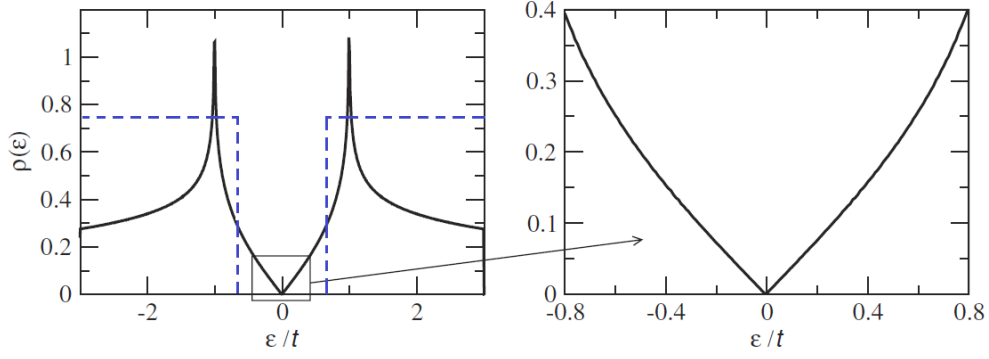


**Figure 1.7.:** [39] Density of states per unit cell as a function of energy in units of  $t$  (overlap energy) computed from the energy dispersion relation close to the neutrality point. The blue dotted line shows the DOS of a usual 2D semiconductor with parabolic bands and a band-gap centered in zero.

Another important effect caused by the symmetrical and zero gap band structure is the so called ambipolar field effect. First we have to say that, as graphene is a semiconductor (even with zero band-gap), at  $T=0K$  and without any bias voltage it is an insulator because the bands are completely filled by electrons (the lower) and holes (the upper). When temperature increases electrons (and holes) that follow Fermi-Dirac statistic start to populate the conduction (valence) band and so they become free carriers. Field effect appears when is induced a positive (negative) “gate” potential in graphene that moves the energy Fermi level down (up) respect to the band. For conductivity this effect is more important than temperature because put a gate voltage means translate the Fermi-Dirac distribution rather than raise its tails. Fig. 1.8 shows the conical low-energy spectrum  $E(\mathbf{k})$  indicating changes in the position of the Fermi energy  $E_F$  with changing gate voltage  $V_g$ . The concentrations of holes and electrons are approximately directly proportional to  $V_g$ .

### Bi-layer and Few-layer graphene

Interesting properties are not limited only to the single-layer graphene indeed also bi-layer and few-layer graphene show a different behavior respect to bulk graphite. Bi-layer graphene consists of two single graphene layers shifted with respect to each other so that the B atoms of one are situated directly above the A atoms of the other [15]. This generates an electronic structure that consists of hyperbolic bands, two of which touch at the charge-neutrality point as shown in Fig. 1.9. In trilayer graphene, the stacking of the third layer can align with the first, known as ABA stacking, or further along again, known as ABC stacking. The ABA-stacked trilayer graphene electronic structure contains both linear and hyperbolic bands. But rather than go further with tight binding analysis it is more interesting focus on phenomenological and qualitative behavior. For instance in bi-layer graphene near to K point the bands can be approximated as 2 parabolas. Thus, in contrast with

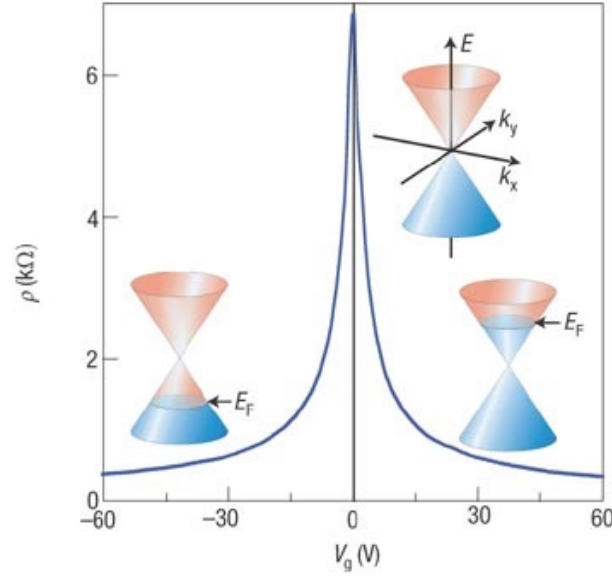


**Figure 1.8.:** [23] Field effect, i.e. resistivity as a function of gate voltage at a fixed source–drain current ( $T = 1$  K). By varying the carrier density via the back gate charge transport is tuned from hole- to electron-like transport by passing the so-called charge-neutrality (or Dirac) point at maximum resistivity. The rapid decrease in resistivity  $\rho$  on adding charge carriers indicates their high mobility (in this case,  $\mu \approx 5000 \text{ cm}^2 \text{ V}^{-1} \text{ s}^{-1}$  and does not noticeably change with increasing temperature to 300 K).

single-layer graphene, charge carriers in bi-layer graphene have finite mass almost like the common semiconductors, furthermore the bandgap of bi-layer graphene is tunable.

### 1.3. Fabrication of graphene

The diffusion of graphene is related especially to his production[40, 10]. When it will be possible to have a huge quantity of high quality graphene, that will be the time of graphene revolution. The mankind started to produce graphene when pencil was invented so many years ago indeed there is graphene in the sign of a pencil over the paper, but it's easy to understand that we are talking about something different. Graphene was first discovered experimentally in 2004 by Novoselov and Geim *et al.* not because they were the firsts to manufacture it, but because they were the firsts to observe it. Their production method was mechanical cleavage where the graphene sheets are mechanically pulled off a piece of graphite by the use of adhesive tape. The result is flakes with a wide distribution in thickness and size. The breakthrough discovery was a simple method to distinguish the single-layer and few-layer flakes from other thicker flakes. It was found that flakes deposited on a 300

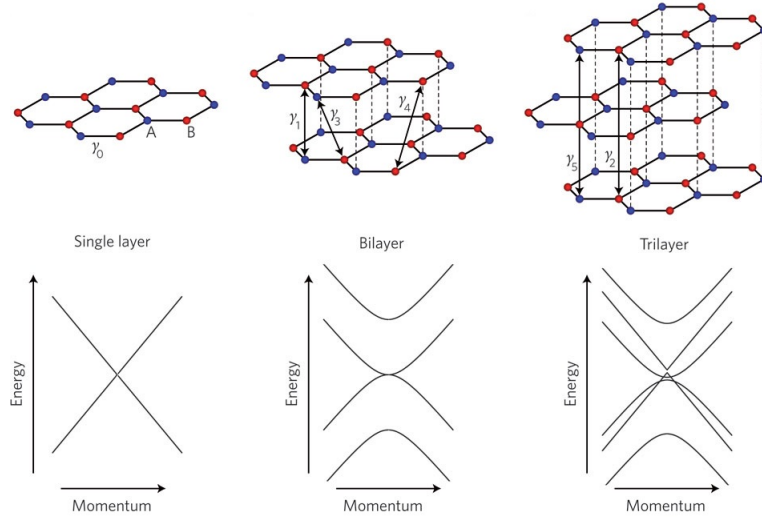


**Figure 1.9.:** Comparison of the band structure obtained with tight binding method between single-, bi- and tri-layer graphene.

nm film of silicon oxide have different color depending on thickness in a standard optical microscope.

After the initial discovery, several different methods have been developed to fabricate graphene. All methods have their advantages and disadvantages. Thus, different methods may be required for different applications (see Fig. 1.10 and Tab. 1.1). The available methods can be roughly summarized into two categories:

- *Bottom-up approaches:*
  - Chemical vapor deposition techniques (CVD)
  - Epitaxial growth on carbides (SiC)
- *Top-down approaches:*
  - Mechanical exfoliation
  - Chemical exfoliation

Using the *bottom-up* approaches, good quality sheets can be achieved. In epitaxial growth silicon carbide is heated to  $>1100^{\circ}\text{C}$  giving thermal decomposition of the material. The outcome is evaporation of silicon and accumulation of carbon at the surface, hence graphene layers are grown. High-frequency transistors based on SiC-grown graphene could replace current MOS transistor technology, hence this kind of production is very interesting for microelectronic devices. One of the most popular way at this moment to manufacture graphene is by using a process called chemical vapor deposition (CVD) [20, 35]. This is a method which can produce relatively high quality graphene, potentially on a large scale. The CVD process allows to create good quality graphene, but it is important to have a good control in parameters

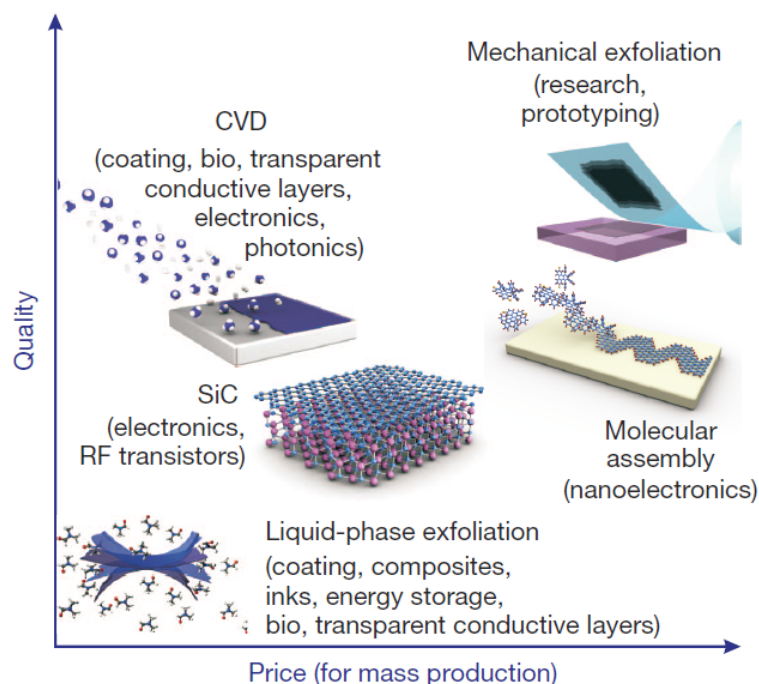


**Figure 1.10.:** The most common methods of mass production of graphene, which allow a wide choice in terms of size, quality and price for any particular application [40].

like gas volumes, pressure, temperature, and time duration of the process. The way CVD works is by combining gas molecules in a reaction chamber which is typically set at ambient temperature. When the combined gases come into contact with the substrate within the reaction chamber (which is heated), a reaction occurs that create a material film on the substrate surface. The waste gases are then pumped from the reaction chamber. CVD graphene is created in two steps, the precursor pyrolysis of a material to form carbon, and the formation of the carbon structure of graphene using the disassociated carbon atoms (which require very high temperature:  $1000^{\circ}\text{C}$  without catalyst). The main problem of this procedure is that at the end of CVD process the substrate must be removed, which is as difficult as the first step. To remove copper substrate (which is one of the most common), it is necessary to dissolve it in a solution and perform many other passages.

We have already mention the first *top-down* approach to produce graphene: mechanical exfoliation. In this way we can produce very good quality graphene, but this isn't a mass-production method so it is useful only for research. Liquid-phase exfoliation of graphite is another. It is based on exposing the materials to a solvent with a surface tension that favors an increase in the total area of graphite crystallites. With the aid of sonication graphite splits into individual platelets, some of those are monolayer graphene sheets. A related method is the graphite oxidation. By oxidizing graphite, the interlayer bonding in the material is weakened and

the resulting graphene oxide sheets can be easily suspended in a polar solvent by sonication. The advantage of having the resulting flakes in suspension is that they can be deposited on many different substrates rather than in only one, as we can do with CVD graphene. Unfortunately, graphene oxide is very difficult to reduce completely back to pure graphene. Ultrasonic-treatment has also been used, often in combination with centrifugation, in order to produce graphene suspensions in organic solvents. However, long sonication times are required: the result is extensive degradation of the hexagonal structure, very small flake sizes and defect formation. Other chemical methods utilize surfactants to dissolve and stabilize graphene in suspension. A problem with the use of surfactants is, however, that they are often difficult to remove and hence can affect the performance of the final products. The challenge in all these methods is to limit the fabrication to single layers: nowadays most of the methods produce a distribution of thicknesses. Lastly, CVD and chemical exfoliation seem to be best candidates for mass-production, but most work remains to be done.

METHOD	GRAINS SIZE ( $\mu m$ )	SAMPLE SIZE ( $mm$ )	APPLICATIONS
<i>Mechanical exfoliation</i>	$> 1000$	$> 1$	<i>Research</i>
<i>Chemical exfoliation</i>	$\leq 0.1$	$\infty$	<i>Coatings, paint/ink, composites, transparent conductive layers, energy storage, bioapplications</i>
<i>CVD</i>	1000	$\sim 1000$	<i>Photonics, nanoelectronics, transparent conductive layers, sensors, bioapplications</i>
<i>SiC</i>	50	100	<i>Hign-frequency transistors and other electronic devices</i>

**Table 1.1.:** Applications of graphene obtained by different methods [40].

## 1.4. Tuning graphene's electronic properties

Graphene has high carrier mobility, higher than every other semiconductor. Its problem is that it is a zero band gap semiconductor, so pristine graphene at room temperature don't behave exactly like a semiconductor. To use graphene in electronic devices it needs some expedients. Particularly now we focus on the use of graphene in field effect transistors to see how important is the capability of controlling and tuning its electronic properties.

In the most common large-area-GFET the carrier density and the type of carrier (electrons or holes) in the graphene channel between source and drain are governed by the potential differences between the channel and the gate [44]. Large positive gate voltages promote an electron accumulation in the channel (n-type channel) and large negative gate voltages promote an hole accumulation (p-type channel, as

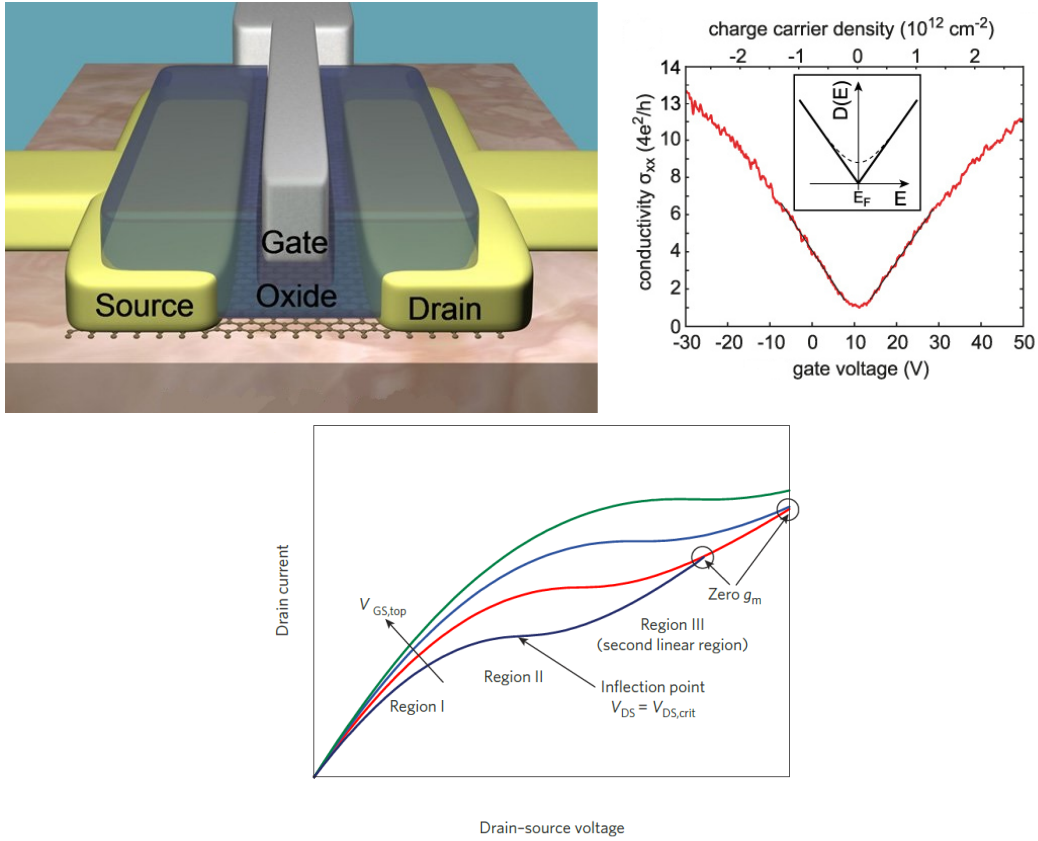


**Figure 1.11.:** 3D view of a top-gated graphene field effect transistor [IBM] on the left and conductivity vs gate voltage on the right. At the bottom qualitative shape of the output characteristics (drain current,  $I_D$ , versus drain–source voltage,  $V_{DS}$ ) of a MOSFET with an n-type large-area-graphene channel, for different values of the top-gate voltage,  $V_{GS}$ . Saturation behavior can be seen. At sufficiently large  $V_{DS}$  values, the output characteristics for different  $V_{GS}$  values may cross.

Fig. 1.8 show). The conductivity

$$\sigma = \frac{Ne^2\tau}{m} \quad (1.7)$$

is directly proportional to the number of carriers  $N$ , thus controlling gate voltage we control the resistance of the channel (see Fig. 1.11). But the aim is to have a large  $\frac{I_{on}}{I_{off}}$  ratio. Silicon CMOS has a on-off ratio of up to  $10^5$ , large area GFET no more than 20. It means that we cannot perfectly switch them off, losing a lot of energy. Here begins the necessity to find other ways to control graphene's bands structure.

In section 1.2 we mentioned that bi-layer graphene has a different band structure from single-layer. As Fig. 1.12 shows, a band gap is opened just applying a voltage [39, 9] in bi-layer graphene and in 2009 Yuanbo Zhang et al. [50] manufactured the first bi-layer GFET. Another approach is try to use narrow graphene ribbons



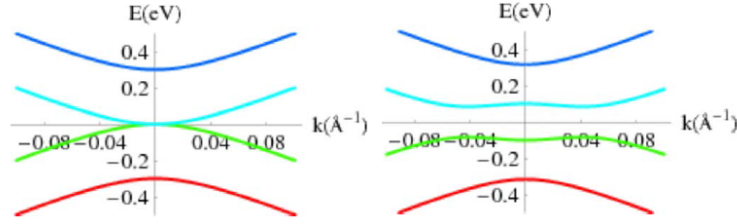


**Figure 1.12.:** Band structure of bilayer graphene of  $V=0$  (left) and  $V\neq 0$  (right).

rather than large area sheets. Ye Lu *et al.* [34] manufactured nanoconstriction field effect transistors (NCFETs) 10nm wide. At this scale the quantum behavior of this ribbon started, showing differences in energy-momentum relation. The result is the formation of a controllable band gap function of the width of the ribbon. The problem is that it is not very easy controlling this width.

Doping [22] is another way to control the gap as is done in semiconductor industry. The substitution of carbon atoms opens a band gap but has a terrible handicap. One of the most interesting properties of graphene is its ballistic charge transport: by introducing defects in its structure we lose this main feature. The method we decided to study in this thesis is the functionalization of the graphene by depositing molecules upon its surface. A detailed description is presented in the next paragraph.

## Functionalization

Functionalization of graphene is of crucial importance for its application in science and technology particularly to tune the Fermi level and open the band gap [26]. Graphene functionalization can be classified in *covalent* and *non-covalent* approaches.

*Covalent functionalization* of the chemically inert plane of graphene requires highly reactive reagents. This low reactivity can be explained by the thermodynamically unfavorable disruption of the  $sp^2$  hybridized network upon functionalization. Also kinetically, covalent functionalization is prevented. The reaction requires the formation of high energy radicals on adjacent carbons atoms, leading to a high energy transition state. Graphene edges and structural defects are much more reactive compared to the bulk plane. Although chemical functionalization of the edges has no significant effect on the electronic properties of large area graphene, it can be used to tune the physical properties of graphene nanoribbons. Organic molecules can be covalently attached to graphene via several chemical routes. One commonly used group of compounds are the aryl diazonium salts. Upon heating, the diazonium salts form highly reactive free radicals that attack  $sp^2$  hybridized carbon forming a covalent bond. In a report by Tour et al., the doping effect of covalently bound diazonium salts with electron donating and electron withdrawing groups was investigated [41] (Fig.1.13). Covalent functionalization is in particular useful for

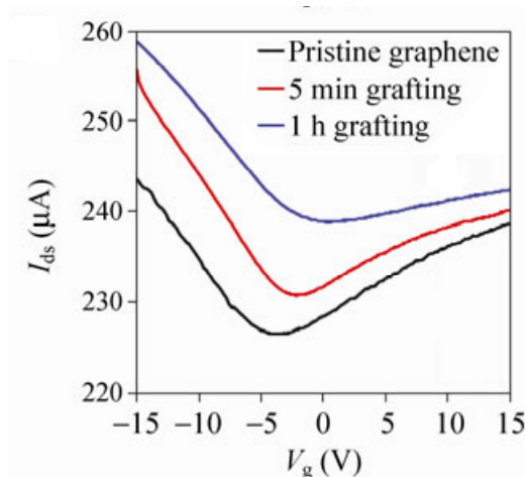


**Figure 1.13.:** Characteristic of a functionalized GFET with diazonium salt. The lines with different colors refer to different time of treatment [41].

opening a band gap, binding recognition elements for sensor applications or dispersing graphene sheets in organic solvents or water. Only p-type doping has been reported upon covalent addition, indicating that the doping effect is mainly caused by the transition from  $sp^2$  to  $sp^3$  hybridization. Covalent functionalization offers the same problems as substitutional doping:  $sp^3$  bonded species inherently result in charge carrier mobility degradation due to defect scattering and the chemical reactions are in general difficult to control.

*Non-covalent functionalization*, also known as physisorption, is governed by relatively weak van der Waals interactions between the substrate and the adsorbate [22]. The strength of these interactions depends on the balance between attractive forces (dispersive, inductive and electrostatic interactions) and repulsive forces (exchange repulsion). An important class of adsorbates are the aromatic compounds. These compounds adsorb strongly on the graphene surface via  $\pi$ - $\pi$  interactions. Theoretical computations show that the interaction between polycyclic aromatic hydrocarbons and the graphene substrate is totally dispersive for distances further away than 4.5 Å from the graphene plane, while at the equilibrium distance ( $\approx 3.5$  Å) it is a complex combination of dispersive and electrostatic interactions.

Besides  $\pi$ - $\pi$  interactions, aromatic compounds bearing electron withdrawing or donating functional groups can have strong charge transfer interactions. These compounds withdraw electrons from graphene or donate electrons to graphene upon adsorption depending on the position of the HOMO/LUMO levels. In general, if the LUMO level of any molecular adsorbate lies below or close to the Dirac point of graphene the adsorbate acts as an electron acceptor (p-type doping), while if the HOMO level lies above or close to the Dirac point it will act as an electron donor (n-type doping). Due to the low work function of graphene (-4.6 eV), n-doping is more difficult to achieve than p-doping. The amount of charge transferred per molecule depends on the exact separation of the HOMO/LUMO levels with respect to the

Dirac point, and the orientation and distance of the adsorbate with respect to the graphene plane. In contrast to covalent and substitutional functionalization, non-covalent functionalization does not disrupt the  $sp^2$  hybridized structure of graphene and thus does not greatly affect its charge carrier mobility. This major advantage compared to the other two approaches makes non-covalent functionalization an excellent approach for tuning the Fermi level (doping) of graphene.

Graphene can be doped by the adsorption of gasses, atoms and organic molecules. Under ambient conditions there is always some degree of doping due to adsorption of species from the atmosphere, especially adsorption of water molecules is attributed to the unintentional p-doping of graphene. Besides molecules, also atoms are capable of charge transfer doping. Alkali atoms, like potassium, are very strong electron donors and form bonds with ionic character resulting in n-doping of graphene. However, the distribution of metal atoms is often inhomogeneous and the charge carrier mobility degrades upon adsorption due to the increased charged-impurity scattering. Organic molecules are the most versatile surface dopants. This versatility opens the possibility of controlling the doping effect via the careful design of the chemistry and geometry of the molecules. Organic molecules can be deposited from solution (spin-coating) or by sublimation from gas phase. The most extensively studied organic dopant molecule is tetrafluoro-tetracyanoquinodimethane (F4-TCNQ)[16, 11]. This molecule is a strong electron acceptor often used as p-type dopant in organic electronic devices. The results of this studies show that the Fermi level is progressively lowered upon increasing the layer thickness of deposited F4-TCNQ (see Fig. 1.14). These molecules like others studied in the past [12] form amorphous, disorganized

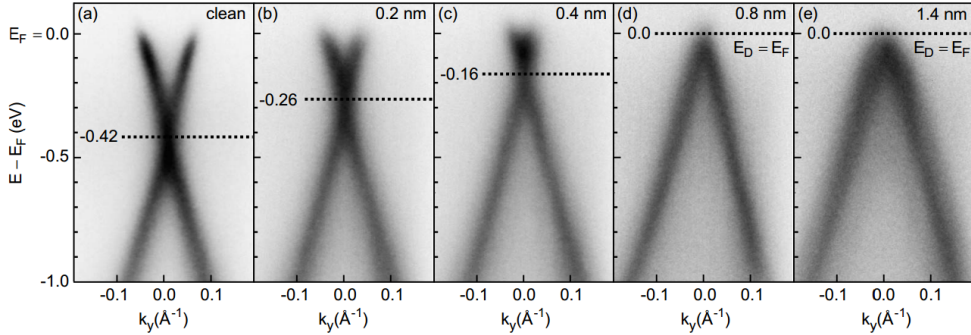


**Figure 1.14.:** Dispersion of the bands measured with UV-excited ARPES of the graphene Brillouin zone for (a) graphene monolayer on SiC and [(b)-(e)] for the same sample covered with an increasing amount of F4-TCNQ molecules. The Fermi level  $E_F$  shifts progressively toward the Dirac point with increasing nominal thickness of the deposited F4-TCNQ film[11].

films on graphene at room temperature. However, there are also adsorbates that organize themselves in well defined ordered structures (see Fig. 1.15). Forming crystalline 2D structures of molecular building blocks on the graphene surface could enable better control in terms of surface concentration, layer thickness and molec-

ular orientation. And as devices are getting smaller and smaller there is a growing need for controlled graphene functionalization by uniform, pin-hole free structures. The name of these organized systems are physisorbed *Self-assembled Monolayers*. Molecular self-assembly is the spontaneous organization of molecular building blocks in well-defined ordered structures via weak, reversible interactions. These processes are governed by non-covalent intermolecular interactions that drive molecules into a stable, low energy state. In this thesis we studied in detail the organic networks first on pristine gold substrate, then on CVD graphene transferred on the same gold substrate to analyze the tuning in surface electronic properties of the material.

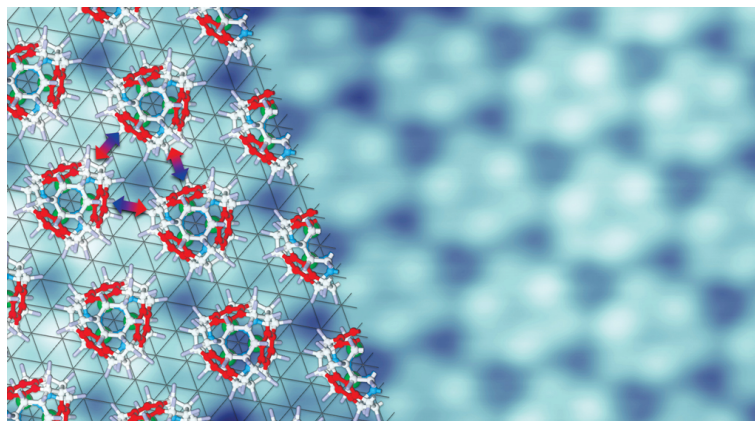


**Figure 1.15.:** Two-dimensional fluorinated fullerene forms SAMs on gold[46].

## 2. Introduction to Scanning Probe Microscopy

*“If you want to make atomic-level manipulations, first you must be able to see what’s going on”. Richard Feynman, 1959.*

A detailed investigation and characterization of the local properties of nanoscopic structures is of great importance for the understanding of novel physical phenomena at the nanoscale. A unique tool for the study of such structures are scanning probe methods, developed in the early '80s. The general idea of the scanning probe microscopy techniques is to use a very sharp tip to “feel” rather than “see” the object to be imaged. These methods allow to obtain atomic scale information in both topographic and spectroscopic measurements at surfaces. Fig.2.1 shows a general

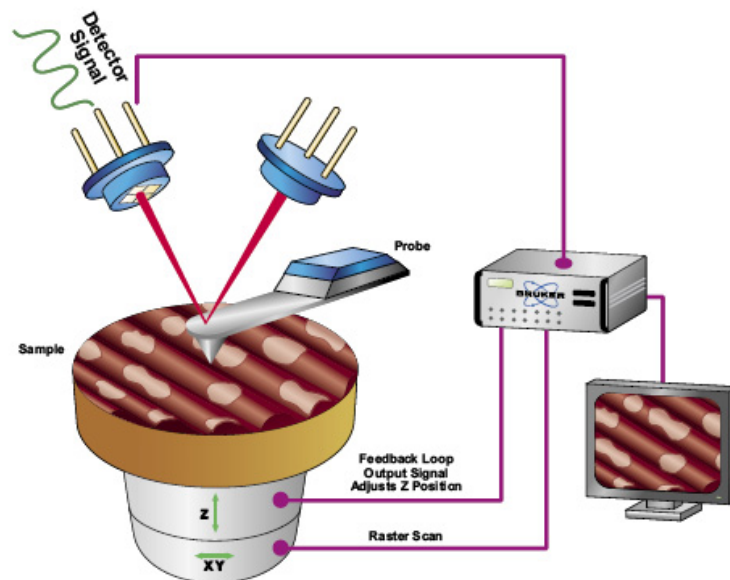


**Figure 2.1.:** General setup of a scanning probe microscope. We can see the sample on a piezoelectric scanner, the tip of the probe that interacts with the surface of the sample, a detector (in this particular case of an AFM) that measure displacement or other parameters of the probe, the electronic module and a computer as user interface.

configuration of a SPM setup. The working principle of all probe microscopes is similar: a sharp probe or tip is brought sufficiently close to a sample surface until a tip-surface interaction is detected. This tip-surface interaction differs depending on the scanning probe that is used. For example, STM uses quantum tunneling between tip and surface whereas AFM detects the mechanical contact force and van der Waals force. Next, the tip is moved following a raster pattern across the sample surface as shown in Fig. 2.2. As the tip-surface interaction strongly depends on the actual tip-surface distance, the signal received will be directly related to the sample topography, and the probe-surface interaction will be recorded as a function of position: recording these data allows to visualize the sample topography. The displacement of the tip plays an important role in a scanning probe microscope. If one wants to investigate small areas on a surface, the tip or sample should be moved with increments of only a fraction of an inter-atomic distance. To ensure an accurate lateral and vertical displacement, the tip and/or sample are placed on a piezoelectric scanner. A piezoelectric actuator generates a mechanical deformation in response to an electric potential. By applying the correct voltage, the sample or tip can be moved by a fraction of a nanometer to several microns in the X-direction, Y-direction or Z-direction. The quality of the piezoelectric scanner ensures the possibility to travel across a sample surface with the accuracy needed for detailed examination of the surface properties. The experimental methods described in this

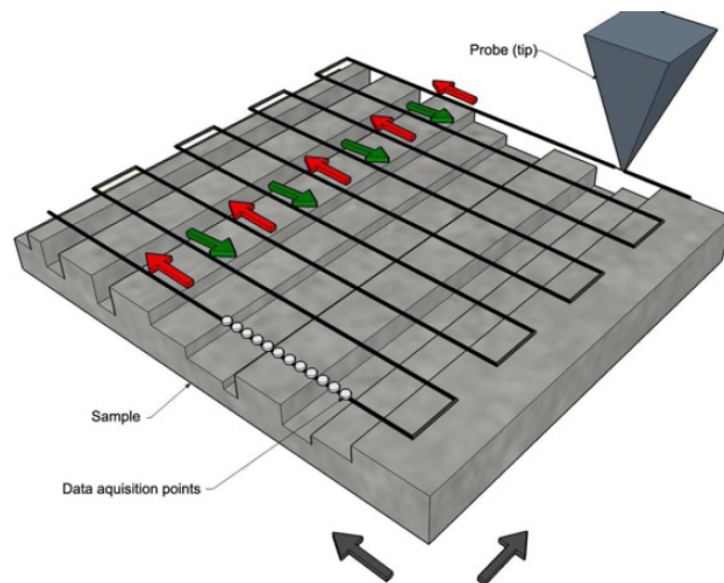


**Figure 2.2.:** Lateral sample scanning (x and y axis) with the probe. The final topography image is later reconstructed from the line by line scanning information.

chapter focus on the two most common SPM techniques: the scanning tunneling microscopy (STM) and the atomic force microscopy (AFM). The sec.2.1 discusses the general operation principle of the STM and theories of the tunneling current. The sec.2.2 discusses the AFM working principle, the physics of the interaction



forces involved, the operation modes and an AFM variant, the Kelvin probe force microscopy (KPFM).

## 2.1. Scanning Tunnel Microscopy

The STM is, quite simply, a fundamental tool indispensable to the development of nanotechnology. The scanning tunneling microscope was developed at IBM Zurich in 1981 by Gerd Binnig and Heinrich Rohrer [3] who shared the Nobel Prize for physics in 1986 because of the microscope.

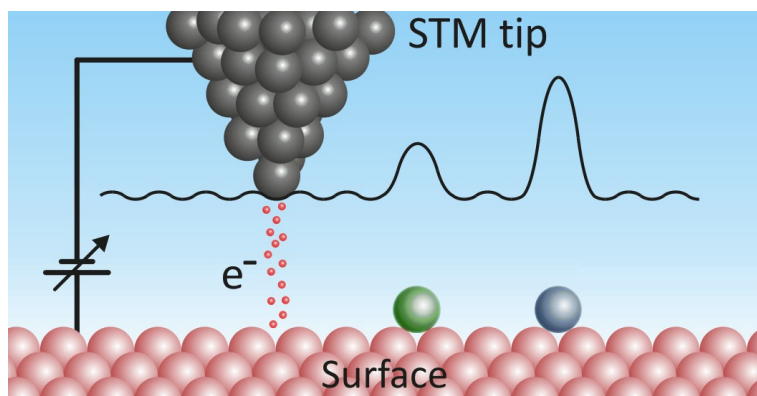


**Figure 2.3.:** Schematic picture of tunneling current between the tip and the surface.

STM is based on the quantum mechanical tunneling effect [47]. The basic operation principles are sketched in Fig. 2.3. A metallic tip is positioned extremely close above a conductive or semiconductive sample, which is mounted on a piezoelectric scanner. Because of the small tip to sample distance, the wavefunctions of the sample and the tip overlap. By applying a bias between sample and tip, electrons can tunnel through the vacuum barrier. The measured tunneling current depends on the local density of electronic states (LDOS) close to the Fermi level of the sample. Under constant current feedback, the STM tip traces approximately the constant *integrated LDOS* surface, since the total tunneling current at a tip position (x,y) is given by

$$I(V_b, x, y) \propto \int_0^{eV_b} \rho_t(E - eV_b) \rho_s(E, x, y) T(E, V_b, Z) dE \quad (2.1)$$

where  $V_b$  is the bias voltage (defined as the sample bias with respect to the tip),  $\rho_t$  and  $\rho_s$  are the tip and sample DOS, respectively,  $E$  is the energy, and  $T$  is the transmission coefficient. At bias voltages  $V_b > 0$  electrons flowing from the tip into the sample are responsible for the current, while at  $V_b < 0$  the direction of the current is reversed. Furthermore this is an approximation because here it is described the STM tunneling process by treating the tip as a single atom, and use

a wave function with a spherical symmetry and a constant DOS for the tip in the energy interval of interest.

By differentiating the tunneling current and assuming an energy independent transmission function and tip DOS, one obtains

$$\frac{dI}{dV_b}(V_b, x, y) \propto T(eV_b, V_b, z) \rho_s(eV_b, x, y) \rho_t(0) \quad (2.2)$$

we can see that the measured  $\frac{dI}{dV_b}$  is directly proportional to the LDOS of the sample at the position of the STM tip. This very important result forms the basis for all scanning tunneling spectroscopy (STS) experiments, in which the  $\frac{dI}{dV_b}$  signal is interpreted as being proportional to the LDOS of the sample with atomic spatial resolution (see Fig. 2.4). The microscopic interpretation of the measured LDOS in a single particle picture in terms of individual wavefunctions  $\psi_i$  at energy  $E_i$  is given by

$$LDOS(eV_b, x, y) = \sum_{\partial E} |\psi_i(E_i, x, y)|^2 \quad (2.3)$$

where  $\partial E$  is the energy resolution of the experiment. Therefore measuring the current and its derivative allows us to know the local probability density to find an electron in that particular place, and if our precision is smaller than bonds dimensions, we will have the picture of how atoms are arranged on the surface.

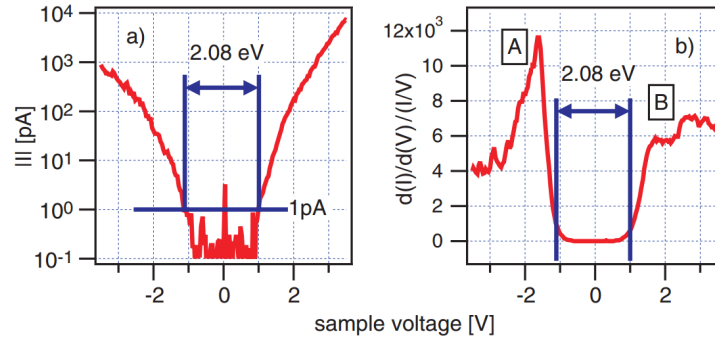


**Figure 2.4.:** Scanning tunneling spectroscopy of a GaSe on n-type silicon: (left) absolute value of the current as a function of tip-sample voltage, and (right)  $\frac{dI}{dV_b}$ , which is proportional to the density of states. A surface band-gap of 2.08 eV is determined [43].

The two most common operation techniques for STM measurement are *constant current mode* and *constant height mode*. In *constant current mode* by using a feedback loop the tip is vertically adjusted in such a way that the current always stays constant. As the current is proportional to the local density of states, the tip follows a contour of a constant density of states during scanning. A kind of a topographic image of the surface is generated by recording the vertical position of the tip. In



*constant height mode* the vertical position of the tip is not changed, equivalent to a slow or disabled feedback. The current as a function of lateral position represents the surface image. This mode is only appropriate for atomically flat surfaces as otherwise a tip crash would be inevitable. One of its advantages is that it can be used at high scanning frequencies (up to 10 kHz). In comparison, the scanning frequency in the constant current mode is about 1 image per second or even per several minutes.

## 2.2. Atomic Force Microscopy

The Atomic Force Microscope (AFM) is the most versatile member of the family of scanning probe microscopes. It was developed by G. Binnig together with Calvin Quate and Christoph Gerber in 1986 [4], five years later the invention of STM. For single crystals also AFM are capable of resolving surfaces with true atomic resolutions, as was shown in the case of the AFM for the first time in 1995 by Giessibl [18], resolving individual atoms on a single crystal Si surface under Ultra High Vacuum (UHV) conditions. Since then the AFM has evolved enormously, and its diversity and versatility enable applications in many different areas of research. It is estimated that in 2012 there are approximately 15,000 AFM's in use around the world. The possibility of applying AFM imaging under both ambient and liquid environments, has been of great importance also for biological applications. In 2000 they go further measuring single orbitals of Si, thus scanning with sub-atomic resolution [19]. While the STM was the first scanning probe technique capable of obtaining atomic resolution, one of its limitations and major disadvantage is that has difficulties to measure *non conducting surface*. This is not a limitation of the AFM, which in principle is applicable to any substrate, including insulating materials, in particular metal oxides. Atomic resolution was presented for the first time on a insulating surface by Reichling and co-workers in 2001 [2]. The following sections describe in detail the basic concepts behind AFM in particular the principles of operation and the physics involved.

AFM measures the forces between a tip and the surface we are scanning. There is a cantilever that bends thanks to the interaction of the tip and the sample. The method to detect the displacement consists of using a cantilever with a reflecting top: on this reflecting top a laser beam is positioned to be reflected on a detector. By measuring the small changes in the reflected laser dot one can deduce information about the sample topography. The movements of the position of the dot on the detector are referred to the instantaneous position of the tip. While the tip is scanning the surface, it feels a force  $F_t$  with the sample surface due to their interaction. This very small force causes a bending of the cantilever that for short displacements can be considered as an ideal spring with force constant  $k$ , according to Hooke's law:

$$F_t = -k\delta_t \tag{2.4}$$

with  $\delta_t$  the displacement of the tip perpendicular to the substrate. With this beam deflection technique can be detected variations of the tip height as small as  $0.1\text{\AA}$ .

The forces that arise between the tip and the surface and that cause the deflection of the cantilever can be classified into attractive and repulsive forces [45]. For attractive forces, van der Waals interaction, electrostatic and chemical forces are included. The repulsive forces can be considered as hard sphere repulsion, Pauli exclusion interaction and electron-electron Coulomb interaction. In general repulsive forces are very short range. The tip-sample interaction is shown in Fig. 2.5.

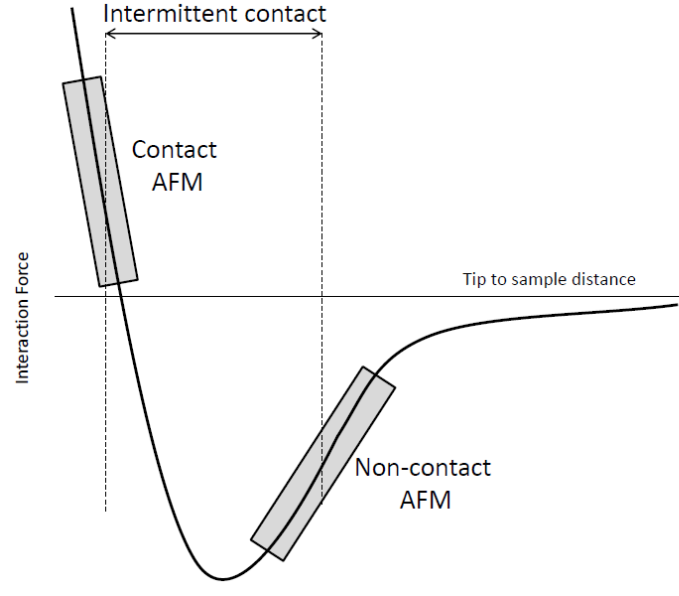


**Figure 2.5.:** The curve shows the typical shape of the tip-sample interacting force.

In nanometer scale long range interactions are those that extend over many atoms dimension. In our case implies that several atoms of the tip interact with several atoms of the surface: this causes a degradation of the resolution. The van der Waals force belongs to this group. The vdW interaction is based on the Coulomb interaction between electrically neutral atoms. Due to finite temperature of the atoms, thermal energy excites the atoms causing deformations in electrons density, that at 0K should be in perfect central symmetry. At a given instant the distortion of the electrons distribution induces an electric dipole in the atom, therefore a dipole electric field. This dipole electric field induces dipole moments in surrounding atoms already in non-equilibrium state therefore a force proportional to  $z^{-2}$  where  $z$  is the distance between the tip and the sample. Another long-ranged force is the electrostatic force. Formally the electrostatic force between two uniformly charged objects falls off with an  $\frac{1}{z^2}$  distance dependence, justifying the long-range classification. If we take into account that here the geometry is very different from two point charges, there is a dependence to  $\frac{1}{z}$  so even more long range.

When two or more atoms come together to form a molecule, the force that tightly

bind the atoms is called a chemical force. In other words, when two atoms are far from each other, the electronic orbitals do not intersect each other (the overlap of the orbitals is vanishing) and no chemical force acts between the atoms. As the atoms are moved closer together the valence orbitals start to overlap, forming molecular bonding and anti-bonding orbitals, and energy is gained by filling valence electrons into the molecular bonding orbitals. This results in an attractive force driving the atoms closer together. At some point the overlap of valence orbitals is optimal, pushing the energy level of the bonding molecular orbital to its lowest possible energy, and the attractive force vanishes. The separation distance where this occurs is also known as the chemical bond length. An attempt to push the atoms even closer together causes a *repulsive force* between the atoms. This because when an atom approaches another atom, the electronic wave function will be overlapped and a very strong force will be generated by nucleus-nucleus repulsion and by *Pauli Exclusion Principle*. An example of a potential that summarize vdW and bond force is the famous Lennard-Jones potential (see Fig. 2.5):

$$V_{LJ} = -4\epsilon \left( \frac{\sigma^6}{z^6} - \frac{\sigma^{12}}{z^{12}} \right) \quad (2.5)$$

where  $\epsilon$  is the depth of the potential well and  $\sigma$  is the distance in which the force is zero.

## 2.3. Experimental setups

In this work we used two different scanning probe microscopes: an AFM for the characterizations of the manufactured samples and a Low-Temperature UHV STM to study the electronic properties of the surface. Now we present in detail these two instruments.

### AFM

The AFMs used for standard topography measurements but also as building block for the KPFM are a commercially available Agilent 5500 SPM. The setup is presented in Fig. 2.6. The setup relies on a scan head with integrated piezo tube and laser detection system. The cantilever is mounted on the piezos scanner and has a maximum scan range of 100 $\mu$ m and 10 $\mu$ m. A high magnification camera is mounted on top of the scan head and provides a top down view of the cantilever and sample. The sample is placed on a movable sample stage that allows motion in the X-direction and Y-direction and in combination with the camera makes it possible to navigate the sample with almost micrometer precision. This navigation ability of the system is especially advantageous for the study of our deposited microscopic

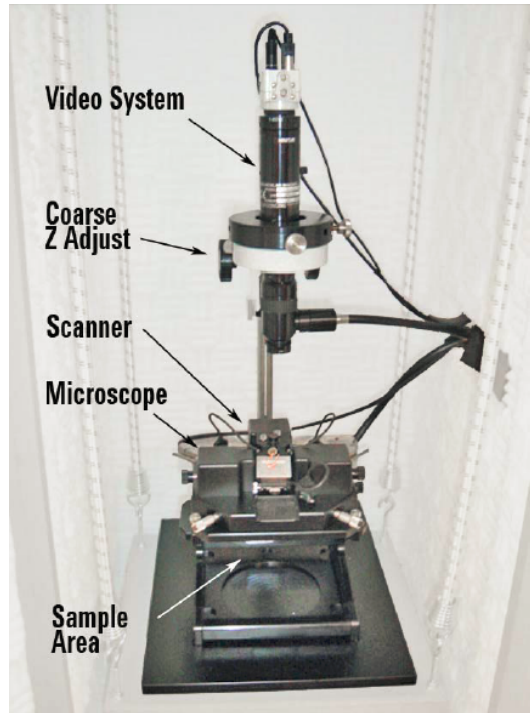


**Figure 2.6.:** Agilent 5500 SPM.

graphene flakes. By using the lock-in amplifier KPFM measurements can be performed. In order to map the surface potential, two different frequencies are applied to the cantilever during the scan: one acoustic usual for topography detection, the second is electrical for SP measurement. Image processing and analysis for STM as well as AFM images was mostly performed by using the free software *Nanotec WSxM*[27].

## Low-Temperature UHV STM

STM and STS measurements were performed with a commercial scanning tunneling microscope (Omicron NanoTechnology). The setup consists of two chambers, the actual STM chamber and a sample preparation chamber, that are independently pumped by means of an ion pump and additional titanium sublimation pump, ensuring operation under UHV conditions at a base pressure below  $5 \times 10^{-11} \text{ mbar}$  in both chambers. The setup is presented in Fig. 2.7. The inset shows a zoom-in view on the scanner and sample stage.

Samples are introduced via a separate load-lock chamber that can be pumped/vented separately from the STM and preparation chamber. Samples are mounted on a large rotational transfer arm that further transports the sample to the preparation chamber and the STM chamber. This transfer arm is equipped with a heater stage to resistively anneal samples *in situ* in the preparation chamber ( $T_{max} \approx 1200 \text{ K}$ ).

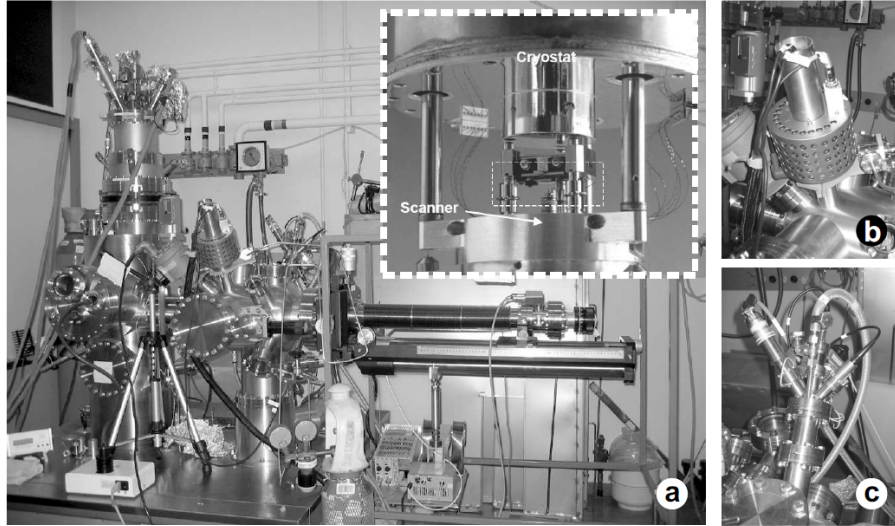


**Figure 2.7.:** (a) The low-temperature ultra-high vacuum STM setup, consisting of the STM measurement chamber and the preparation chamber. Inset (taken from Omicron Nanotechnology): In the STM chamber the scanner and the sample stage are present. The sample can be brought in contact with the cryostat for cooling to low temperatures. The preparation chamber is equipped with (b) an argon ion gun and (c) two evaporation cells.

The chamber is further equipped with an argon ion gun (AG21 from VG Scientific) and two evaporation cells (EFM3 from Omicron Nanotechnology). The microscope is mounted in a thermally shielded compartment directly attached to a cryostat that consists of an inner and an outer part, allowing measurements at room temperature ( $T_{sample} \approx 300K$ ) and at low temperatures. For working at low temperatures, the outer part is filled with liquid nitrogen, while the inner part can be filled with either liquid nitrogen or liquid helium. This way, sample temperatures  $T_{sample}$  of 78K (liquid nitrogen) and 4.5K (liquid helium) can be achieved. For optimal topography and energy resolution, all measurements were performed at 4.5 K, unless indicated otherwise in the text. The time available for STM measurements at liquid helium temperatures without refilling the cryostat is around 24 hours. A spring suspension system with Eddy current damping ensures optimal vibration isolation. The z-resolution of the STM is better than 0.1 nm. The bias voltages  $V$  given in the text and figure captions are always with respect to the sample, while the STM tip is virtually grounded. Setpoint values of the bias voltage  $V$  and tunneling current  $I$  at which the presented topography images were acquired are typically around 100mV and 0.1-1.0 nA, respectively, unless indicated otherwise.



## 3. Sample production and characterization

In the previous chapters we have given the details about the scanning probe techniques and a general view on graphene. Here we present the experimental work done. The gold substrates preparation and characterization is presented in the first section. Graphene transfer process and its preliminary analysis are presented in the second and third section. The detailed study with AFM and STM of graphene transferred on Au(111) is presented in the last section.

### 3.1. Au films on mica

#### Growth and cleaning procedure

An ideal candidate as substrate for atomic resolution STM measurements is the Au(111) grown on mica. Mica surface has atomically flat terraces of over  $1\mu m^2$  in size, but mica is an insulator, therefore it cannot be scan by STM. We grew Au since it is an inert material that can be used in UHV conditions even for some months. The *ex situ* preparation of Au(111) films is made by molecular beam epitaxy (MBE, Fig. 3.1) at high temperatures. The cleaved mica is introduced in a high vacuum load-lock ( $10^{-8}$  mbar) and degassed by annealing during 1 hour at  $T = 550^\circ C$ . For the film deposition an MBE setup with a UHV deposition chamber is used. Gold is deposited by thermal evaporation from a Knudsen cell containing high purity gold (99.999 %). The evaporation rates (typically 0.03 - 0.1nm/s) are controlled by temperature stabilization and calibrated by quartz crystal oscillators. Gold films with large atomically flat terraces are obtained when the substrate is kept at a temperature of  $500^\circ C$  during evaporation and at  $530^\circ C$  during post-annealing for 1 hour. Sample transport from the MBE setup to the LT UHV STM setup is performed under ambient conditions. To remove surface contamination the Au(111) films are cleaned in the preparation chamber of the STM setup by repeated cycles of Ar ion sputtering (4 minutes at 4 keV and  $10^{-6}$  mbar) and annealing (12 hours at 720 K).

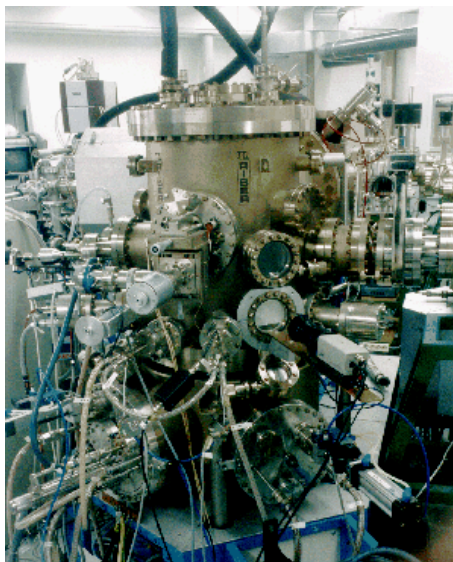


**Figure 3.1.:** MBE setup used for the growth of Au on mica. A big stainless steel chamber keeps under vacuum, connected to the gold evaporator.

### About the surface reconstruction and the surface electrons

Bulk gold has an FCC structure, but the surface shows a different structure called *surface reconstruction* [25, 36]. This is a process of some materials in which atoms of the surface assume a different organization than that of the bulk. In Fig. 3.2 geometric and parallel lines are visible on the flat terraces: this is the so called “herringbone” structure. The lightest lines with lateral periodicity of 6.3nm divide FCC (the wider) and HCP (the narrower) regions. The two areas exhibit differences when we deposit molecules on the surface, showing different affinity to them (for more detail see Chapter 4). Besides its typical topographical features, the Au(111) surface also exhibits intriguing electronic properties [5] like 2D surface electrons waves (see Fig. 3.3 (a)). These delocalized surface state electrons are being confined to the top atomic layers (by the vacuum barrier at one side and at the other side by the sp-band gap in the bulk valence states that is created by the termination of the crystal at the surface) therefore act as a (quasi) two-dimensional free electron gas. The Au(111) surface state was visualized for the first time by Hasegawa et al. in 1993 by means of STM at room temperature [24]. Surface electrons are scattered at step edges, surface defects and impurities and the resulting interference of the incident and reflected electron waves give rise to energy dependent periodic spatial oscillations of the electron density of states at the surface. Since the standing waves occur isotropically along all directions in the surface plane with similar wavelengths, the surface electron state gives rise to a circular two-dimensional contour in the Fourier transform graph. This is nicely visualized in Fig. 3.3(a), presenting a LDOS map at -30meV of a flat terrace, several nanometers away from any step edge. The corresponding Fourier image in Fig. 3.3(b) reveals a quasi perfect circular



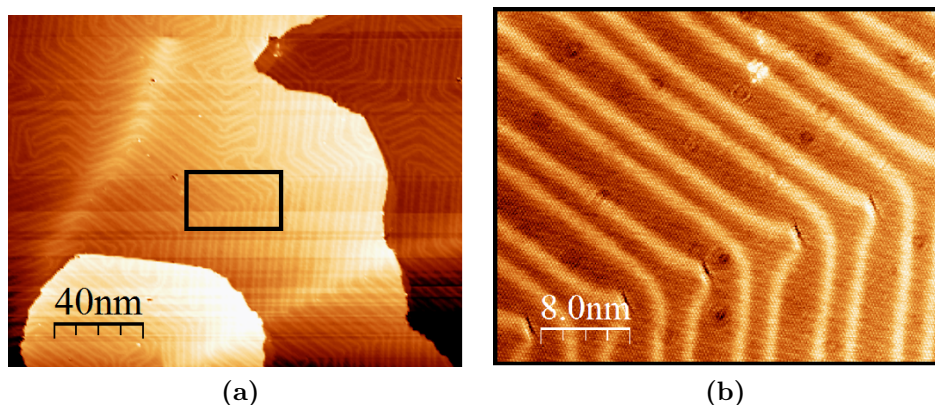


**Figure 3.2.:** (a) STM image with three different atomically flat levels of the gold surface are visible. (b) Zoom in the black rectangle of (a) image, herringbone structure is clearly visible.

Fermi contour, indicating that only a limited range of wavelengths is contributing to the standing waves [42]. The experimental observation around the Fermi level is consistent with the expected parabolic behavior of a quasi 2D free-electron-like gas

$$E(k_{\parallel}) = E_0 + \hbar^2 k_{\parallel}^2 / 2m^* \quad (3.1)$$

where  $E_0$  is the onset energy of the surface state and  $m^*$  is the effective electron mass which take into account the potential variation parallel to the surface [30] (Fig. 3.3 (c)).

## 3.2. Graphene growth and transfer

At the present Chemical Vapor Deposition is the less expensive known technique for mass production of good quality graphene sheets. The CVD graphene used for this experiment was made by dr. C.D.Wang in the Department of Physics and Material Science of the City University of Hong Kong with the setup in Fig. 3.4. Cu and Ni foils are considered to be excellent substrates for making high-quality graphene films with uniform thickness due to the low solubility of C in Cu and Ni since in the nineties graphite was already grown on these materials. In contrast to Ni, exceptional results in terms of uniform deposition of high quality single layered graphene over large areas have been recently achieved on polycrystalline copper foils [32]. Detailed imaging and spectroscopic analysis have revealed that over 95% of the copper surface is covered by single layered graphene while the remaining graphene is 2-3 layers thick, independently from growth time or heating and cooling rates. The process involves the decomposition of methane gas over the copper substrate with a constant flux of  $H_2$ . Graphene films were grown on commercial 25- $\mu\text{m}$  thick Alfa Aesar Cu foils. The typical growth process is:

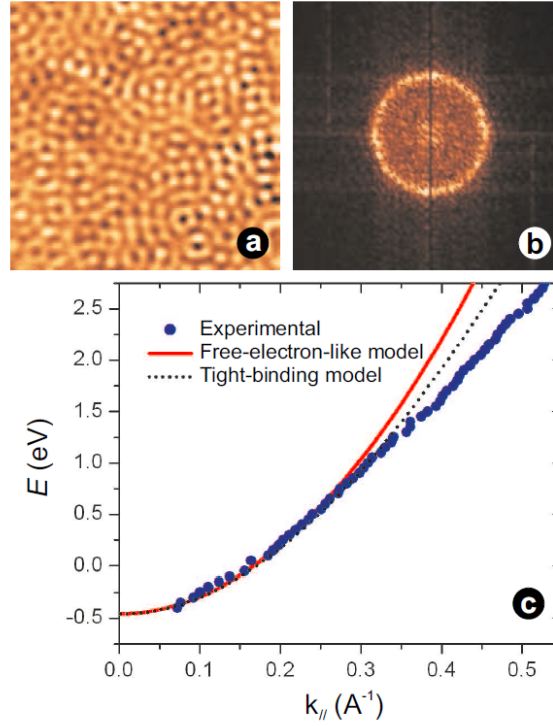


**Figure 3.3.:** (a) 35.3nm x 35.3nm LDOS map at -30meV of an Au(111) terrace. (b) The corresponding Fourier transform image makes clear that only a narrow range of wave vectors contribute to the observed standing wave patterns. (c) Plot of the electron energy  $E$  as a function of the parallel wave vector  $k$ , as determined from the Fourier transformed LDOS maps at various bias voltages  $V$ . Data are fitted to the free-electron-like model and a tight-binding model [30].

1. clean Cu foil in acetone, isopropyl alcohol and deionized (DI) water by sonication;
2. load the fused silica tube with the  $1 \times 1 \text{ cm}^2$  Cu foil, evacuate, back fill with hydrogen, heat to  $950^\circ\text{C}$  and maintain a  $H_2$  pressure of  $10^{-3} \text{ mbar}$  under a 2 sccm flow;
3. stabilize the Cu film at the desired temperatures, up to  $1000^\circ\text{C}$ , and introduce 1.5 sccm of  $CH_4$  and 100 sccm of  $H_2$  for 30 minutes at a total pressure of  $10^{-2} \text{ mbar}$ ;
4. after exposure to  $CH_4$ , the furnace was cooled to room temperature. The cooling rate was  $100^\circ\text{C}/\text{min}$ .

Despite the good results, the CVD process is not completely understood and the quality of the material produced is not yet as good as mechanical exfoliated graphene. The first quality limitation is the presence of grain boundaries formed during the graphene growth but its electronic properties are actually not very compromised by these defects as shown in section 3.4.

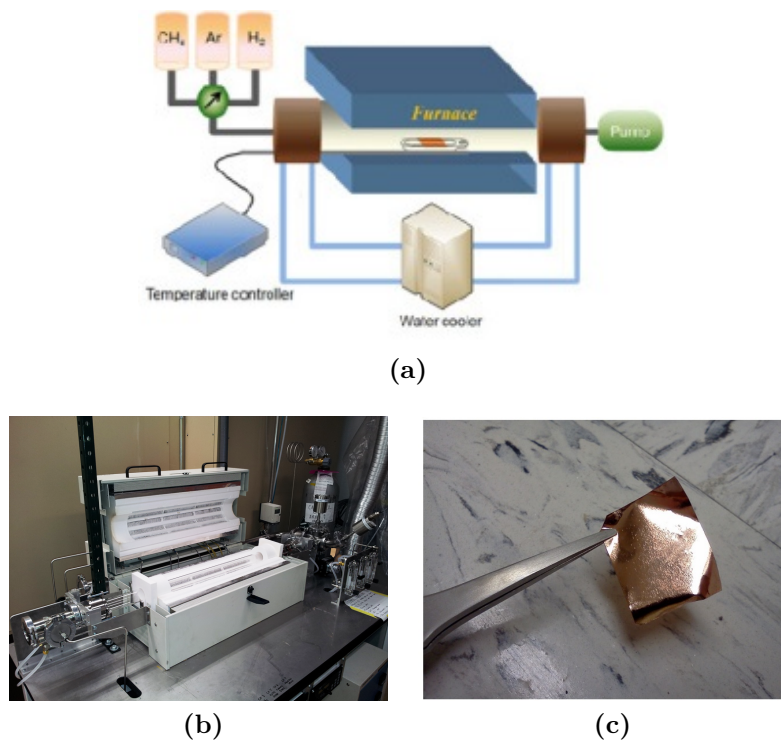


**Figure 3.4.:** (a) Model and (b) photo of the Chemical Vapor Deposition system. (c) CVD graphene on top of the copper foil.

### Characterization of the as-grown graphene

After the deposition we have to confirm the presence of the graphene layer on the surface. The most rapid and sensitive technique is Raman spectroscopy method in which a laser is pointed to the substance to be identified, and then the light subsequently radiated is measured. The light interacts with the phonons in the material, and the energy of the photons is shifted up or down. The wavelengths very close to the initial wavelength of the laser are filtered, as they are just reflections of the material. The rest of the shifts are analyzed to determine which shifts are true Raman shifts, rather than absorption lines. In the general description of the Raman shifts, a photon excites a molecule of the material from the ground state to a virtual energy state and when the molecule relaxes it emits a photon and it returns to a different rotational or vibrational state, which is different from absorption (as with fluorescence) where the molecule is excited to a discrete (not virtual) energy level. This shift is calculated and then often displayed as a graph. Graphene has several very specific peaks when subjected to Raman spectroscopy, therefore this is a quite effective method of identifying its presence. There are three main peaks to take into account in graphene Raman spectra:  $G$  peak at  $1600\text{ cm}^{-1}$ ,  $G'$  at  $2650\text{ cm}^{-1}$  and  $D$  at  $1300\text{ cm}^{-1}$  [14]. The ratio between the height of the  $G'$  and  $G$  peak gives information about the number of layers of the graphene. If  $G'$  is higher

than  $G$ , then there is a high percentage of monolayer graphene in the surface, if it is not monolayer graphene's presence is negligible.  $D$  peak refers to defects: perfect graphene layer spectrum doesn't show  $D$  peak. Unfortunately, Raman spectra of CVD graphene on Cu is not very easy to be studied because it has an intrinsic problem (see Fig. 3.5). The presence of the copper foil appears as a Gaussian background in the graph, then it is more advisable to analyze the spectra of transfer graphene on Si substrate as will be presented in section 3.2. However, Raman spectroscopy

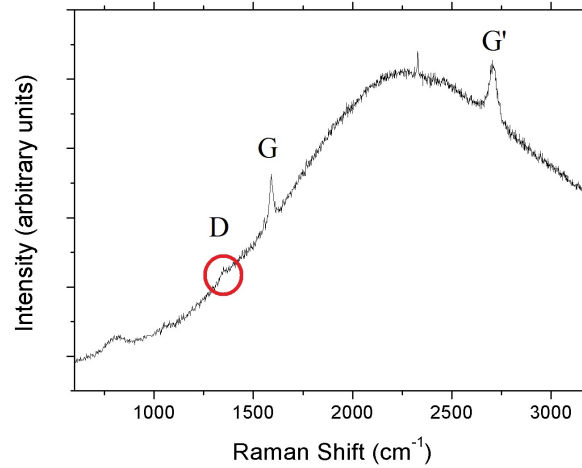


**Figure 3.5.:** Raman spectrum for CVD grown graphene on Cu foil. Despite the Gaussian background due to the presence of copper,  $G$  and  $G'$  peaks are clearly visible and  $D$  peak is small compare to them, which suggests not many defects in the mono-layer lattice.

is a non local measurement, indeed its signal is an average of the photon emission energy of all the area irradiated by the laser beam, which is at least of some square micrometers. For our purpose it is necessary a more local characterization, therefore the technique most suitable for us is scanning probe microscopy. The first approach to the sample is with *Agilent* AFM (see section 2.3) which allows an immediate measure without particular treatments and a relatively large scale scan range (tens of microns). Fig. 3.6 shows the results. The roughness is around 50 nm but the surface is not homogeneous at all at this scale. At best, 250 nm x 250 nm flat grains can be seen. The surface is dominated by the structure of the copper, thus the presence of graphene cannot be confirmed by AFM. Before the measurements with *Omicron* STM (see chapter 2 for more details) in ultra high vacuum (UHV) and low temperature (LHe, liquid helium temperature) conditions the sample underwent one-night *in situ* annealing at 700°C to clean the surface from contamination. STM images show that the copper foil is only partially covered by graphene: both a square-like atomic structure (stemming from the copper) and a hexagonal atomic structure (stemming from the graphene, Fig. 3.7a) is revealed. The copper foil seems to consist of (poly)crystalline and amorphous regions. The graphene regions include

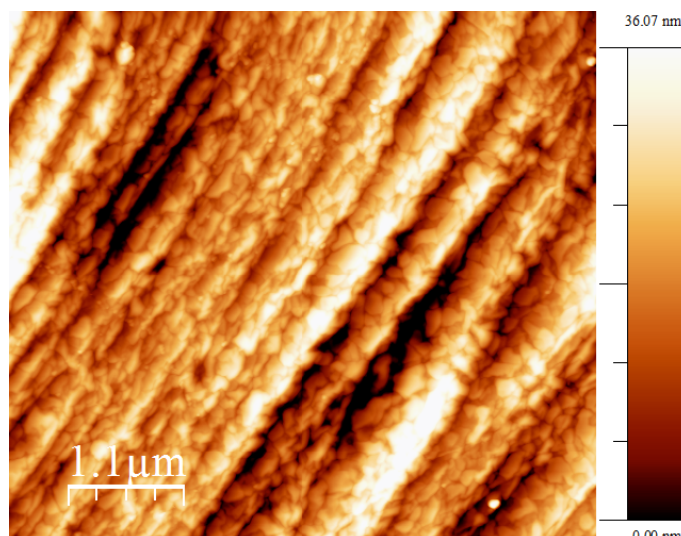


**Figure 3.6.:** 5μm x5μm AFM image of graphene on copper. Graphene layer is hidden by copper roughness.

atomically flat regions, graphene "bubbles" (see Fig. 3.7b) and graphene "wrinkles". The atomically flat graphene regions exhibit additional periodic structure that can be interpreted as a Moiré pattern. Parallel stripe Moiré patterns are likely formed by single-layer graphene and copper, while other more complex patterns may be formed by two stacked graphene layers, indicating the presence of bilayer graphene on the surface.

Locally, atomic size defects can be retrieved. Typically, however, the atomically resolved regions do not exhibit any defects and indicate the high quality of the graphene. STS spectra of the graphene surface show very diverse electronic properties that vary from location to location: electronic states and band gaps can be observed in these "topography singularities". As it was for Raman, but for different reasons, evaluating the quality of our graphene at this step is meaningless because of the intrinsic imperfections of the copper surface. Only after a well done transfer process onto flat substrates it will be possible to infer something. Because of this, every comment concerning the quality of our graphene is postponed to section 3.2.

### Transfer process

One of the hardest parts about working with graphene is moving it from one substrate to another. As it is a single atom thick, sheets of graphene are quite fragile and inclined to wrinkling and tearing. Different groups working on graphene projects use very different methods to transfer it onto the substrate they need. The most common of all of the methods used to move graphene from the metal foil in which it was grown onto another substrate involves a sacrificial polymer layer. The general idea of the transfer is to attach a polymer to the graphene, remove the layers on the



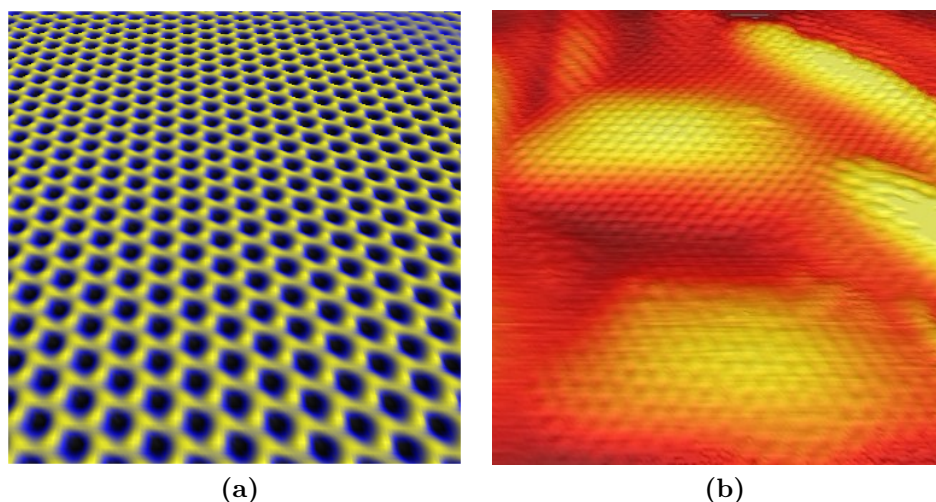


**Figure 3.7.:** (a) 6 nm x 6 nm STM filtered 3D image of atomically flat area. Hexagonal lattice structure is clearly visible. (b) 10 nm x 10 nm STM filtered 3D image, atomically resolved graphene “bubbles”.

opposite side and then deposit it on the desired substrate. A polymer (poly(methyl methacrylate), or PMMA for short) is deposited onto the metal via spincoating. Spincoating is a procedure where a liquid material is laid on the desired substrate, and then it is spun at high speeds. The polymer binds to the graphene on the surface of the metal. We spincoated 10 ml of PMMA for 4 times at 3000 rpm for 60 seconds and after that the polymer must be cured at 150 degrees Celsius. The next steps are used to remove the metal from the polymer and graphene. There are multiple ways to do this, but each method must remove the metal growth substrate. Copper sulfate ( $CuSO_4$ ) works well as an etchant for copper. Once the layer has been removed, the remaining film (polymer and graphene) must be placed onto the desired substrate. All traces of the etchant used must be washed, so the film must be washed in multiple baths of deionized water before being deposited on the substrate. Extreme care must be taken in these steps, as the graphene layer is exposed on the polymer. The washing process is necessary, because the copper sulfate, as a strong acid, would certainly degrade the quality of the final product if left on the film for very long periods of time. The final step of this method is to remove the polymer from the top of the graphene. Depending on the polymer used, different procedures are required, some need heat, while others require an acetone bath. In our case we deposit some drops of acetone and then remove the acetone via spincoating. In this way the displacement of the layer on top of the substrate is prevented. Then we wash with ethanol and then with water. After the water removal, the resulting film should be uniform over the final substrate, but often is not.

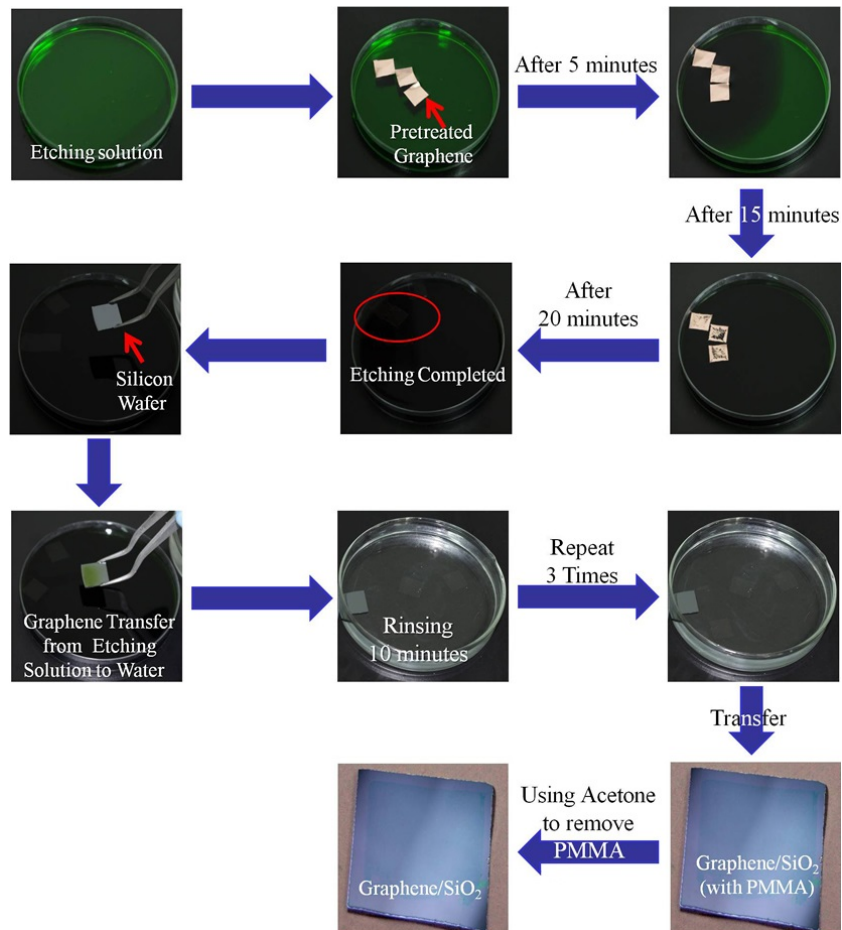


**Figure 3.8.:** Process to remove the copper foil and transfer the graphene layer on silicon wafers (the same procedure can be used with gold substrates).

### 3.3. Graphene on SiO<sub>2</sub>

Graphene has been transferred in two different kind of substrates: Si wafer with 300 nm of SiO<sub>2</sub> on top and Au(111) grown on mica (which will be discussed in section 3.4).

In Fig. 3.9 it's clearly visible a layer on top of the surface. It is not trivial that graphene is visible because it is actually transparent. The only reason that makes graphene visible is a combination of some particular features of the substrate. The most common substrates which allows this are silicon wafers with 300 nm of oxide. A famous article by P. Blake *et al.* [7] explains how this mechanism works. Their idea is to solve the problem with geometrical optics: in the approximation they assume a totally reflecting surface (the interface silicon-silicon oxide) and two transparent media (the silicon oxide and the graphene) with two different complex refractive indexes. In this way it is straightforward to show how the light interferes differently in the regions where there are graphene respect where there are not.

We start the analysis just by watching the sample with the naked eye. The reflection on the surface is uniform both where graphene is and where it is not. The layer is visible only at some angles, and at that angles some regions appear of a different color (arrow in Fig. 3.9a) which could be due to a folding of the layer.

In Fig. 3.9b under optical microscope it is possible to confirm that different color are due to different number of layers caused by the folding of the graphene sheet during the transfer process. The white arrow shows the area with two layers, the black arrow shows the one with three layers. Apart from the folding, the surface is no uniform at all: there are many micrometer size tears. These tears could be a problem for devices, but for our purposes they are negligible.

At length Raman has been discussed in section 3.2. Differently from the previous measurement, now graphene is on a silicon wafer which doesn't display any particular effect in Raman spectra, therefore in these new data only information of graphene can be found. Fig. 3.9c clearly shows that G' peak is higher than G peak: this means that monolayer graphene is present. D peak, which arises from disorder in  $sp^2$  hybridized carbon systems, is one order of magnitude lower than G so defects in honeycomb lattice are rare. Actually there are the possibility that a big contribution in G peak's rising was done in the transfer process because in Fig. 3.5 it really seemed smaller. The sample doesn't need any special preparation for the measurements with the *Agilent* AFM. The images was taken running the *tapping operation mode* in which the AFM cantilever is vibrated near the surface of the sample (see section 2.2). The tip is brought close to the sample so that at the bottom of its travel it just weakly hits, or tap, the sample. This mode is less likely to damage the sample than the more usual *contact mode* in which the tip really dig the surface, because it eliminates lateral forces between the tip and the sample. In this way we prevent to cause tears during the scanning since graphene layer is quite fragile.

Fig. 3.10(a) shows a micrometer-size scan which reveals many features of the sample. First the red spots: these are contamination, likely caused by a not perfect removal of the PMMA or acetone. But they are not so dense to influence our purpose, so they are negligible.

Focusing on the tone of the blue, it is clearly visible that the background is light blue, but there are some darker islands. It means that these islands are few nanometers higher than the rest. To explain their presence we must take into account the formation process of the graphene, which is in fact chemical vapor deposited graphene (CVD). During the formation process, the single layer starts to nucleate in different nucleation sites. The layer is grown since all the surface is covered, this implies that in the nucleation sites a second layer starts to growth before the ending of the process. We can state that our continuous graphene layer is approximately 50% bilayer. The blue islands are 2 nm higher than the light blue background, in other words the step on the corner of the islands is 2 nm. It is more difficult to find a clean step between the silicon and the first graphene layer, because often it is too much rough and dirty. The profile of the only plausible step we found is reported in Fig. 3.10(b). The lower blue line refers to the level of the silicon, the line in the middle to monolayer graphene and last one to bilayer. In literature [13] is reported that exfoliated



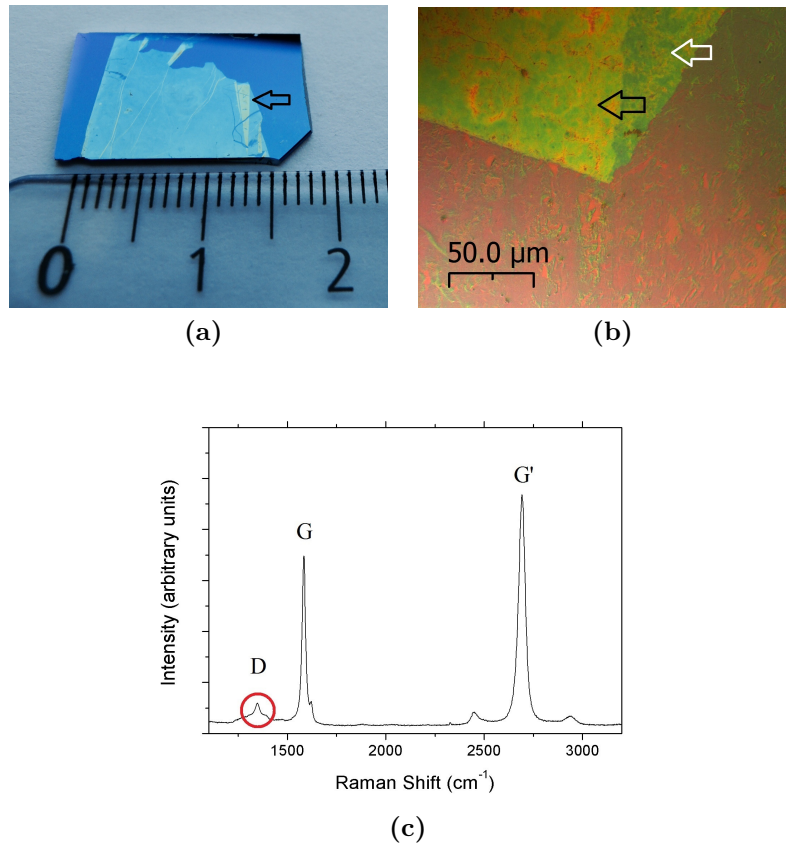


**Figure 3.9.:** (a) Graphene on silicon wafer. (b) Folded sheet of graphene under optical microscope. (c) Raman spectrum of graphene on silicon.

graphene on silicon oxide should be around 1.22 nm high. Our graphene is almost twice, but it was expected because, due to the transfer process that is performed under water, there must be a water layer trapped between graphene and silicon. The third interesting feature of this sample is the presence of narrow wires on the surface. We can think the graphene layer as a cloth which covers the substrate. Using this similarity we can easily understand what these narrow lines are: wrinkles of the cloth [51] randomly distributed. More detail will be presented in STM measurements.

### 3.4. Graphene on Au(111)

STM's samples must be conductive since the intrinsic measurement method (see section 2.1) requires a flux of charge carriers between the tip and the sample which is, actually, exactly the signal needed to explore the surface in detail. In principle it is possible to measure graphene even on silicon oxide (which is an insulator) because graphene is conductive, but only if the layer is continuous, and this is a condition

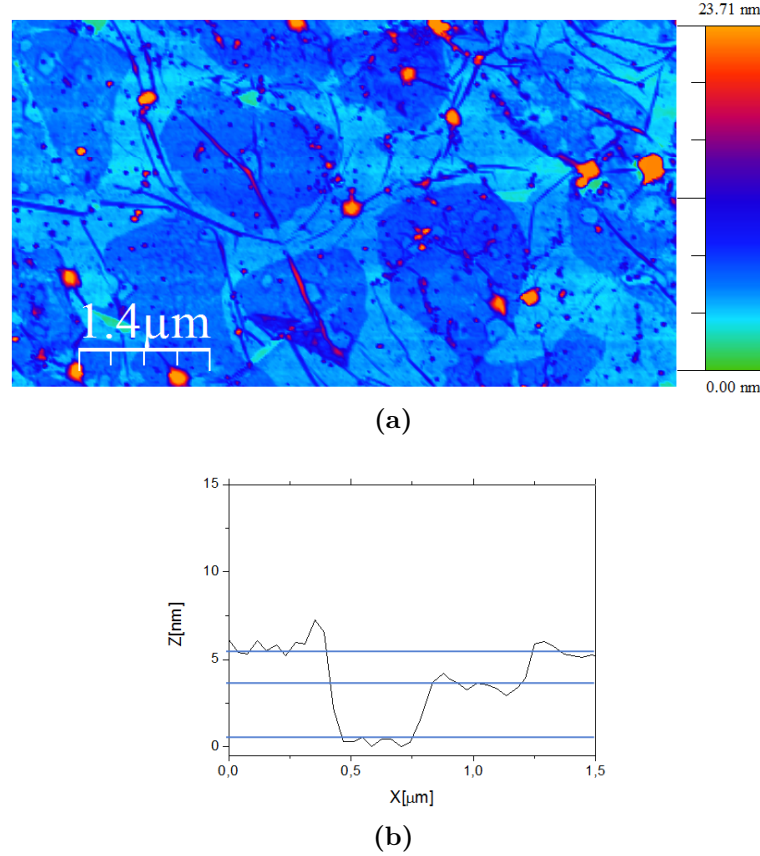


**Figure 3.10.:** (a) AFM image of graphene on silicon. Darker blue islands reveal the presence of bilayer graphene. (b) Three level profile of silicon, first and second layer of graphene.

that is not always satisfied. For this reason we transferred it on top of Au(111) grown on mica. The detail of this surface are described in sec.3.1. This surface is not as flat as silicon oxide surface, but it is a good compromise.

The transfer process is the same used for silicon. Fig. 3.11(a) shows one of the two samples manufactured. Even with the naked eye it's visible a rectangular transparent layer that covers almost all the surface of the sample, but in this case, differently from Fig. 3.9(a), there are no particular optical effects. The only reason why we can recognize the boundary of the graphene is that the boundary itself is a defect.

Before the main measurement with the *Omicron* UHV STM we checked the surface with the *Agilent* AFM. Fig. 3.11(b) is the most significant result. The white spots are just contamination due to *ex situ* transfer process or, more likely, chemicals not completely removed from the surface. At first sight, a part from those contamination, the sample really seems to be pristine gold on mica, without any layer on top. But if we look more carefully we can recognize (black arrows) irregular lines on top of the flat terraces, which are clearly something not usual in gold images. We ascribe

these imperfections to the presence of graphene, since they exist also in Fig. 3.10(a). Differently from Fig. 3.10(a) no bilayer islands are visible even if graphene is the same, but we can easily state this is because irregularities of the gold surface are comparable (or even smaller) with the size of the islands.

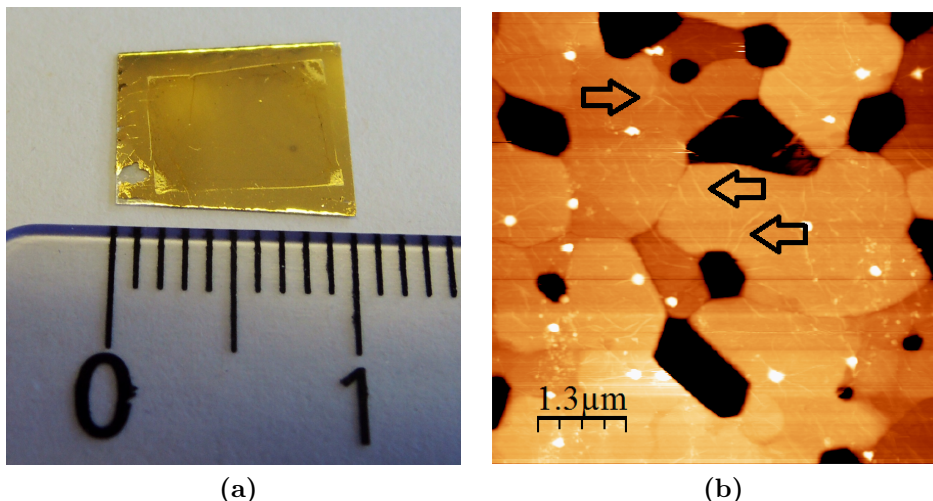


**Figure 3.11.:** (a) Photo of graphene transfer on gold (the transparent rectangular layer in the middle of the sample is graphene). (b) AFM image of graphene on gold.

After the characterization with AFM, the sample was ready for UHV low-temperature STM. Our sample must be vented and then placed in the preparation chamber of the setup (see Fig. 2.7). Once there it is subjected to annealing at 400°C for 10 hours. Annealing is useful to clean the surface from contamination which should evaporate, but, at these temperature, it induces also a reconstruction in the gold. It is possible that the presence of a layer on top of the gold changes its final structure. Preliminary measurements are taken at liquid nitrogen temperature ( $\sim 77$  K) with a home-made Platinum Iridium tip. Liquid nitrogen temperature allows large scan range ( $> 1\mu\text{m}$ ) which are necessary to confirm the quality of the sample. But at this temperature the surface shows some instability, almost like a resonance effect of the graphene layer forced by tunneling current, nevertheless it is possible to obtain atomic resolution. In order to perform more confident measurements, we cool it down to liquid helium temperature ( $\sim 4$  K) always with PtIr tip which demonstrated to behave better than Tungsten tip.

In literature there are many examples of graphene's scanning probe microscopy on Au(111) [8, 49], but ours is the first UHV LHe STM and STS attempt of transferred graphene on gold. The transfer process is difficult, being able to obtain a sample good also for UHV and LHe standard is even more challenging.

Firsts large scale images show the same features seen with AFM: corrugation of the graphene layer (Fig. 3.12a). The shape and the height of our wrinkles is the same

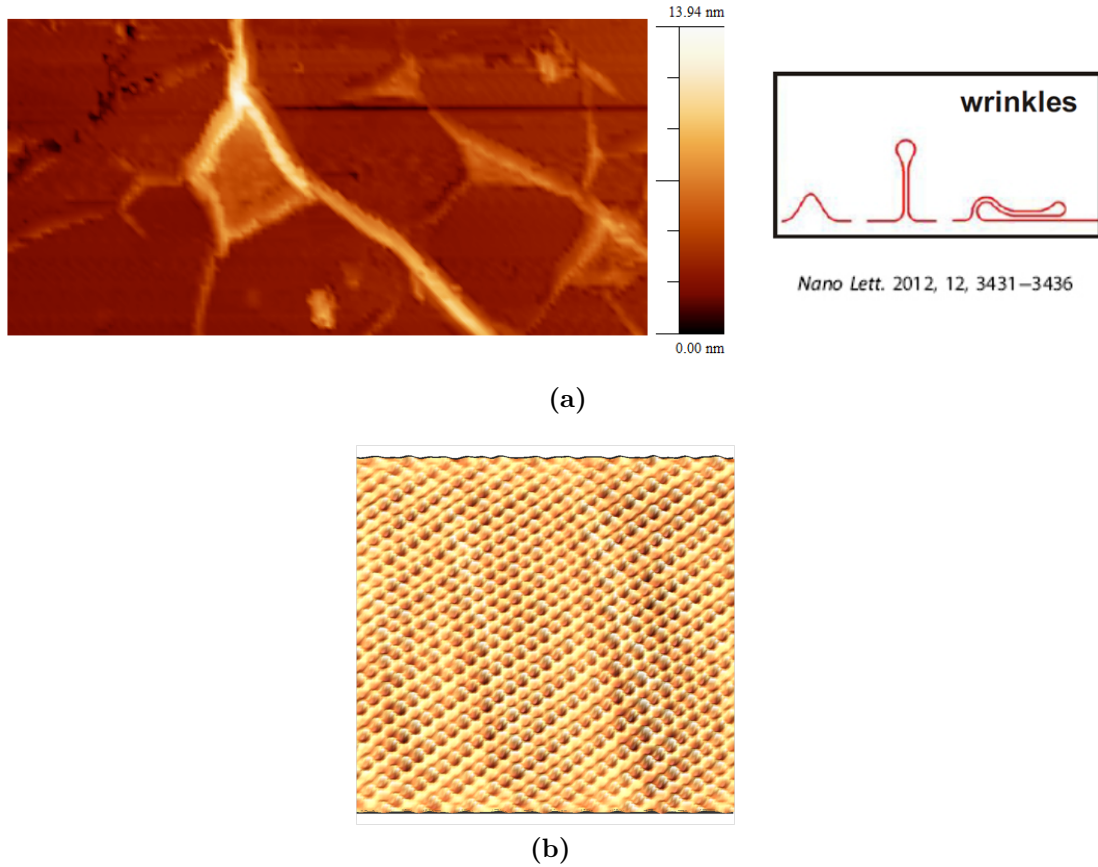


**Figure 3.12.:** (a) Graphene “wrinkles” viewed by STM and their hypothetical shape. (b) Not filtered STM 3D image of graphene lattice.

reported by Wenjuan Zhu *et al.* in 2012 [51]. Our work is not focused on wrinkles, but this is an additional confirmation of a good graphene layer. Another topography peculiarity is the atomic step of the gold. Au(111) grown on mica displays atomically flat terraces, divided by 0.2 nm steps, which is in fact the height of a layer of the gold atoms. These steps are sharp but the graphene round them, thus the passage between the two level of the gold appears very spread. As a conclusion to this microscopic analysis it can be stated that locally clean areas can be retrieved, on which perfectly atomically flat regions are separated from each others by different surface peculiarity like wrinkles and gold steps.

Focusing on the flat regions one of the most satisfying results is atomic resolution. Fig. 3.12(b) is a not filtered 3D image of the honeycomb lattice taken at 4 K. To get the better possible resolution, scanning parameters must be set carefully. This particular scan is performed with 2.1 nA of tunneling current, 0.1 V of bias voltage and the speed of the scanner is 10nm/s. With these particular setting the tip is relatively close to the surface because the current is high and the voltage is low, comparing with standard measurements, even the speed of the scanner is quite slow.

At opposite settings the images appeared very unstable, and no honeycomb lattice is visible. The main disadvantage in scanning so close to the surface is that it could happen to pick up a small graphene flake with the tip. In this case the tip cannot be improved any more with usual tricks, so it must be replaced.

As expected, gold suffered a different surface reconstruction, rather than the usual herringbone structure, now the HCP and FCC regions are divided by long parallel lines. This changing is for sure due to the presence of graphene which changes the surface energy conditions. Carrying on the exploration we come across a defect that we interpret as a grain boundary (Fig. 3.13a). In section 3.2 the growing process has been discussed. It is well known that our graphene starts to nucleate in different places until these different islands touch themselves forming grain boundaries, thus they are not unexpected. There are two main evidences of this theory. The first is that the defect (diagonal line in middle image, Fig. 3.13a) is not caused by gold surface because horizontal parallel lines in both sides confirm that below the graphene layer gold is homogeneous. The second is a different orientation of the graphene lattice. To state this we don't check directly the relative orientations of the two lattices (on the right and on the left) which is actually difficult because atomic resolution so close to a defect is not always reached, but another effect which is even more straightforward. The major proof is the presence of Moiré pattern only in one side (Fig. 3.13a, bottom images).

Moiré pattern is a well known effect in graphics, it appears when two patterns (identical or different, no matter) are overlaid while displaced or rotated a small amount from one another. This overlapping can produce a new pattern with larger periodicity, depending from the relative rotation. In our system we have gold pattern and graphene pattern. The only difference between graphic Moiré pattern and the Moiré pattern we see on STM images is that the first one is just a visual effect (an artifact), the second one is a true electrons wave functions superposition which causes a stable signal during the scanning that appears as a periodic pattern [6].

Then, what can be the conclusion? The two sides are of the same height, there is only this diagonal line in between and Moiré pattern in only one side: this must be a grain boundary caused by the growing process.

A step like the one shown in Fig. 3.10b in order to confirm the presence of bilayer islands isn't imaged because STM scan range is too small. Nevertheless there is another unequivocal proof of that. Fig. 3.13b(left) shows the most strange feature found. It is possible to recognize the honeycomb atomic structure, but also other two patterns with larger periodicity. It is more clear if we focus on Fig. 3.13b(right) which is the Fast Fourier Transform of Fig. 3.13b(left), *i.e.* the reciprocal lattice.



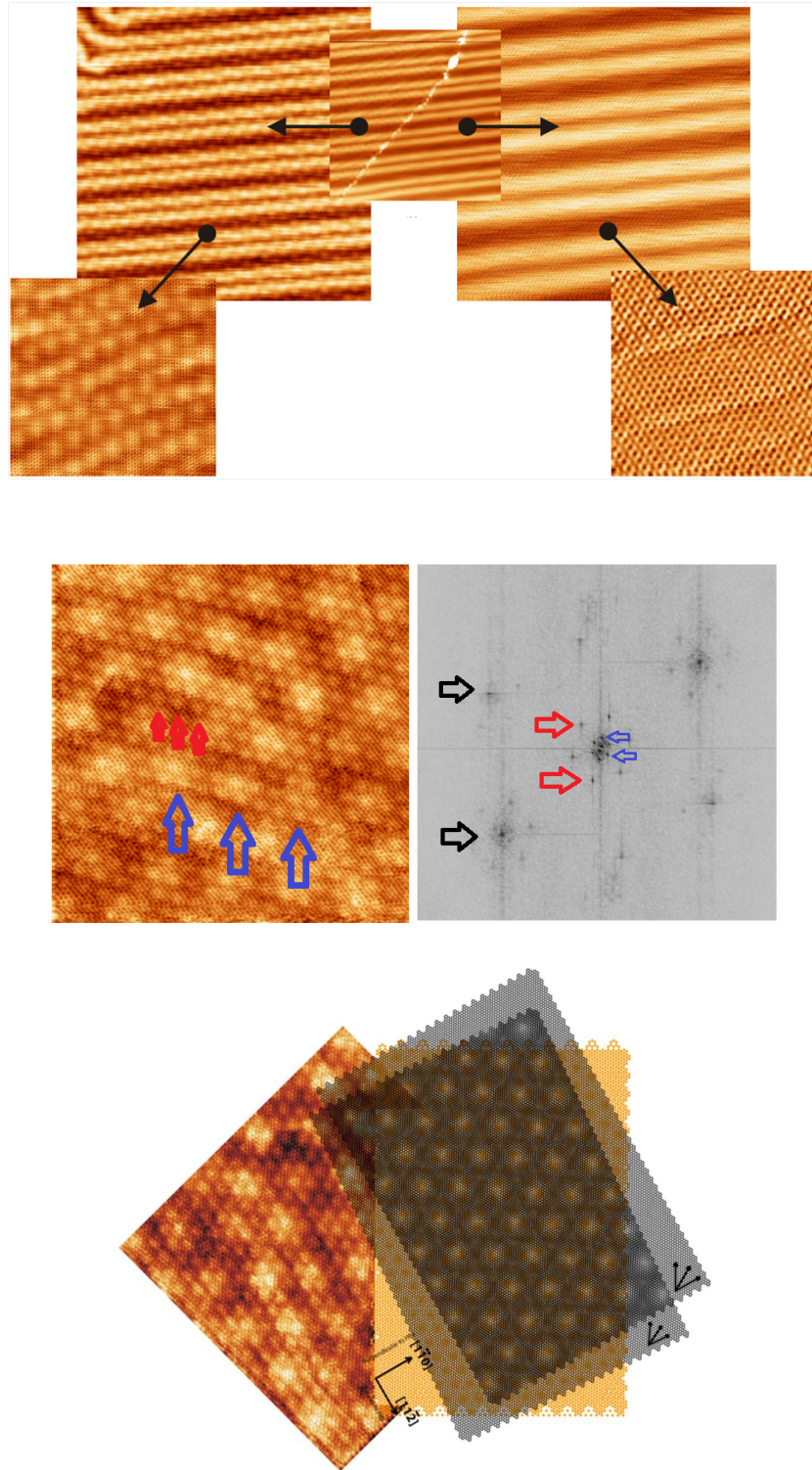


**Figure 3.13.:** (a) A grain boundary. Arrows displays a zoom in the two sides of the grain, the lowest images are filtered in order to show the presence (left) and the absence (right) of the Moiré pattern. (b) Double Moiré pattern in a bilayer region and its Fourier transform. Arrows show the three periodicity of the image. (c) Simulation of the double Moiré pattern.

Black arrows point to the group of six dots which refers to the atoms periodicity (they are not reported in left image). Red arrows refer to the second hexagonal group which represents the smaller pattern in left image and then blue arrows point the dots very close to the center which are the reciprocal vectors of the bigger pattern in left image. There is only one explanation of this fact, as Miller *et al.* reported in 2010 [37]: rather than the relative twist of only two layers which causes standard Moiré pattern, here there are the relative twist of three layers that causes this double Moiré pattern. The three layers are: the gold surface, the first and the second graphene layer. There exists a way to simulate optically what we see. Superimposing three layers, one with circles in HCP like on gold, and the other two with honeycomb stacking like graphene, obviously with the right proportion, we can try to get the same patterns. Then just by twisting two layers we tried to match the simulated image with the measured one and we succeeded. The conclusion is that the first layer of graphene and the gold has a relative twist of around  $28.5^\circ$  between  $(1\bar{1}0)$  direction of gold and  $(11\bar{2}0)$  of graphene, the angle between the first and the second graphene layer (between  $(11\bar{2}0)$  directions) is around  $1.5^\circ$ . The topography analysis is concluded, now it will be presented some spectroscopy, which is a direct observation of the LDOS. STS measurements require several hours of scanning, constant condition of temperature and low vibrations, that's why this measurements are often performed during the night. The resulting data are a set of  $I(V)$  and  $dI/dV(V)$  curves for every point of the grid defined before the measure, which can contain a thousand of points. In Fig. 3.14 there is the comparison between the theoretical expectation for pristine graphene LDOS and an average of  $dI/dV(V)$  (which is actually the LDOS) curves of a 5 nm x 5 nm flat region without any defect of our graphene on gold. The red vertical line represents the Fermi level. On pristine

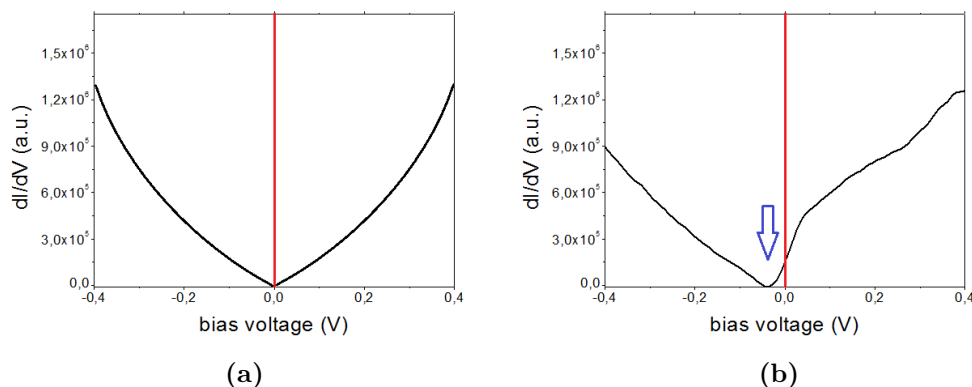


**Figure 3.14.:** (a) Theoretical LDOS and (b) measured LDOS, the blue arrow points to the Dirac point.

suspended graphene the theoretical expectation is a V shaped curve centered on the Fermi level which means, a part from temperature deviation, no electrons in conduction band and no holes in valence band. There should be a perfect symme-

try. What we observe is different. In almost every measure we always recognize a tendency for the minimum to move a bit through negative values: the apex of the V, called Dirac point, is always below the Fermi level. What does it mean? Our idea is that gold can supply electrons to graphene, in this way its conduction band become populated. Gold is like a dopant for graphene, the result is a n-doped graphene. The other big difference between theoretical and measured LDOS is the asymmetry of the curve, but to go deep in details DFT calculations are necessary.



## 4. Molecules physisorption

Two-dimensional molecular networks on various surfaces are receiving much attention, one reason is the prospect of potential applications, for instance, their ability to tune the properties of the surface below. In this chapter we first present the molecules we have used, the DBA-OC<sub>4</sub>. In the second section molecules deposited on gold are discussed and in the third section their behavior on graphite.

### 4.1. DBA-OC<sub>4</sub>

Alkoxyated derivatives of triangular dehydrobenzo[12]annulene (DBA) are provided by Prof. Kazukuni Tahara from the Department of Advanced Materials Science of the University of Tokyo [29, 28]. The core of these molecules has triangular shape with benzene rings on vertices with two alkoxy legs attached (OC<sub>4</sub>). The planar shape of the entire molecule is shown in Fig. 4.1. OC<sub>4</sub> refers to the composition of the legs: one oxygen (red atoms) and 4 carbons. The theoretical arrangement should form a honeycomb two dimensional lattice like Fig. 4.1(c). There are two orientations of the hexagonal rings, clockwise and counterclockwise, but they should be equally probable.

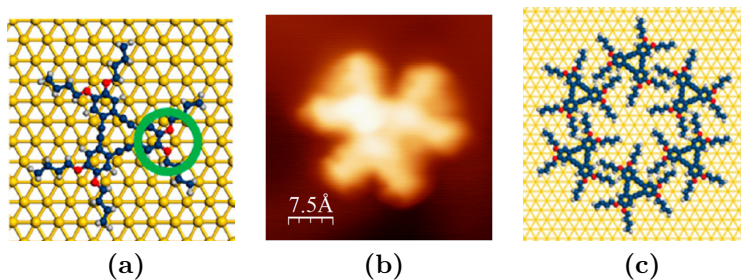


**Figure 4.1.:** (a) Adsorption model of DBA-OC<sub>4</sub> on the Au(111) surface. Green circle indicates the surface molecule interaction between O atoms of two butoxy groups and Au lattice. (b) STM best resolution for DBA-OC<sub>4</sub>. (c) The hypothetical honeycomb structure of DBA-OC<sub>4</sub> formed by the chain–chain vdW interactions.

## 4.2. DBA-OC<sub>4</sub> on Au(111)

The hypothetical structure of DBA molecules on gold is shown in Fig. 4.1(b). Our first aim is to deposit these molecules on gold surface and see how they arrange. In order to do that we use a Knudsen cell linked to the preparation chamber of the UHV STM. In vacuum condition the molecules is heated up to their evaporation temperature (207°C), at this point they exit the Knudsen cell and hit the clean Au(111), since the sample is at ambient temperature they remain attached to the surface. Then the sample is brought to the main chamber of the setup: all STM measurements were performed at Ultra-high vacuum and Helium temperature.

We start with 1 minute deposition. The result is a low coverage (Fig. 4.2). No networks like Fig. 4.1(b) are visible, only individual molecules are present. The main feature of these molecules is that they are not planar (see Fig. 4.2c) but there is a vertex of the triangular clearly higher than the other two (white definite spot is higher than the other paler two), thus single molecules don't behave like Fig. 4.1(a). These molecules are unstable at higher voltages and current (in Fig. 4.2(b) see the instability in some of them) and they have preferences for FCC regions of the Au(111) reconstruction. The instability is something that can be controlled and transformed in manipulation. In fact just by applying an high voltage to the white spot of a molecule, this suffers a tilting and the result is that the vertex lowers and the another lifts (see Fig. 4.2c, d, e). Lock-in images (Fig. 4.2f, g) which show the LDOS at fixed voltages (*i.e.* energy) are very interesting because forcing the unoccupied energy levels by scanning at high voltages we can populate orbitals which are not populated in normal conditions. In this way Fig. 4.2f, g are taken and particularly at 3.5 V we can see an unexpected shape of this orbitals which have, rather than triangular symmetry as molecules have, hexagonal symmetry. After this single molecules observation we deposit for other 5 minutes to reach a higher coverage. Actually the density per surface area increases a lot, but still no networks appear. Molecules prefer to arrange all along the surface reconstruction of gold forming wire rather than big frameworks. The idea is to anneal the sample (heat it) to make molecules more mobile on the surface and facilitate them to rearrange. The attempt at 100°C failed, probably the temperature was not high enough but at 200°C, very close to evaporation temperature, we succeeded. Fig. 4.3c shows the sample after last annealing. Networks larger than 80 nm with more than a hundred of molecules can be easily found. These networks are more stable than single molecules, only after high voltage scanning (>3.0 V), somewhere, they appear broken. We note that these molecules can arrange in two different ways, they can organize in clockwise but also in counterclockwise rotation, and the two are equally likely.

A famous article published on Science in 2009 [33] suggests to try to find electron bound states in the pores (the empty spaces between molecules): at some energies these pores should work as quantum wells for surface electrons of the gold. Fig. 4.3d, e show the topography and the LDOS at -150 mV. It is perfectly clear that where pores are in topography image, there are excess of electrons shown as white spots

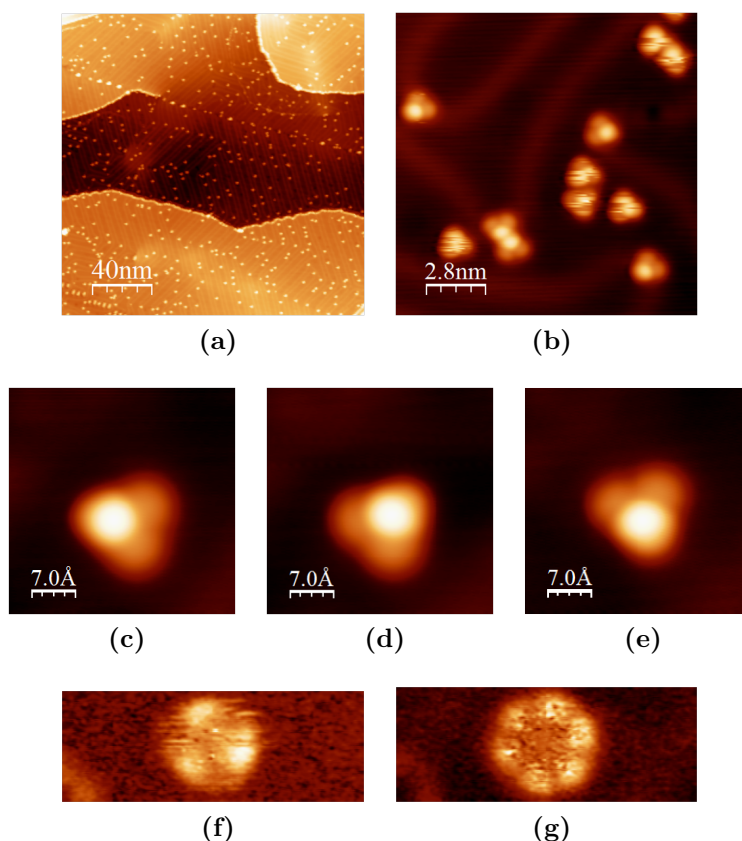


**Figure 4.2.:** (a, b) Low coverage of the surface allows imaging of single molecules. (c, d, e) Controlled manipulation by voltage and current pulses. (f, g) Unoccupied orbitals of a DBA molecule at 3.0 V (f) and 3.5 V (g).

in the LDOS image. This excess can be interpreted as bound states. These states are even more clear in spectroscopy analysis. In Fig. 4.3f is displayed the spectra taken above pristine gold, above the center of a molecule and in the middle of a pore. They appear quite complicated, but there is an incontrovertible evidence of a peak in pore's spectrum at -150 mV which demonstrates what we said before.

### 4.3. DBA-OC<sub>4</sub> on HOPG

Highly Oriented Pyrolytic Graphite (HOPG) is a relatively new form of high purity carbon and provides microscopists with a renewable and smooth surface. Graphite in general and HOPG in particular consist of a lamellar structure, like mica, molybdenum disulphide and other layered materials that are composed of stacked planes. All of these examples of lamellar structures have much stronger forces within the lateral planes than between the planes, thus explaining the characteristic cleaving properties of all of these materials. In an atomic resolution scanning tunneling mi-

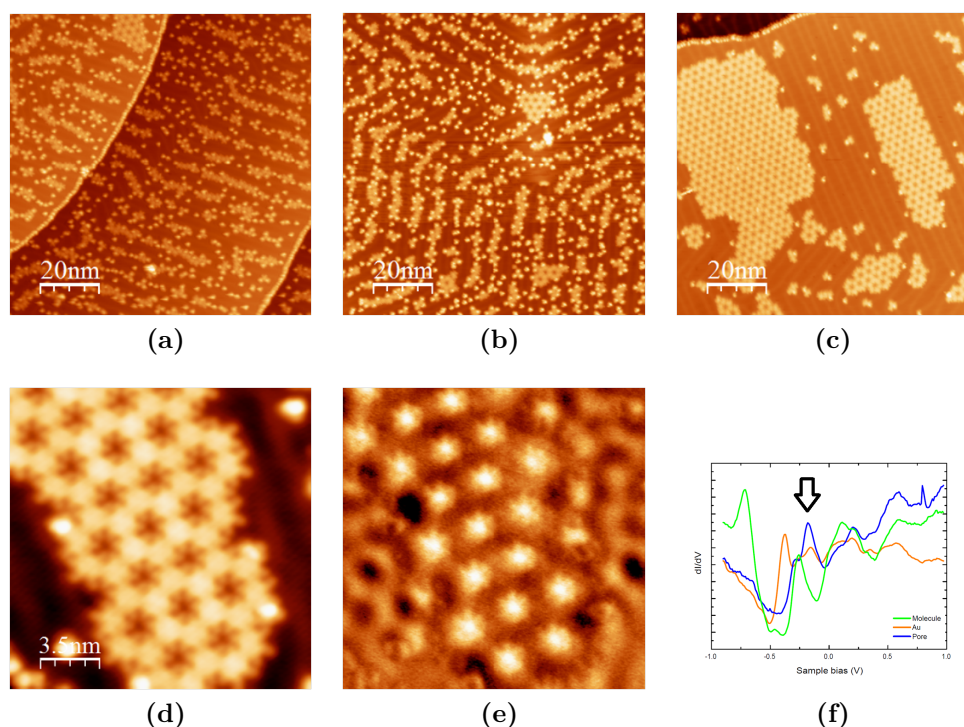


**Figure 4.3.:** Higher coverage (a) without annealing, (b) after first annealing at 100°C and (c) after second annealing at 200°C. STM image of topography (d) and LDOS (e) at -150 mV. (f) STS in different position: above pristine gold, above a molecule and above a pore. The black arrow shows the peak inside the pore.

croscopy image of the graphite structure of HOPG, there are two possible images. The image normally obtained looks like a close packed array; in this array each atom is surrounded by six nearest neighbors (Fig. 4.4b). The distance between any two of these atoms is 0.246 nm. Under ideal tunneling current and tip conditions, we can see the honeycomb structure that shows the hexagonal rings that are the true structure of graphite; the center to center atomic distance in this image is 0.1415 nm. The honeycomb structure is not always visible because on graphite a half of the atoms are bounded with the layer below (see Fig. 1.9) so their orbitals are lower the others and they cannot be imaged. There are only two kind of features on the surface of graphite: steps (Fig. 4.4a) and Moiré patterns. The procedure to prepare the sample involves a cleaving process with a scotch tape. In this way we divide two layers of the sample to get the best cleanliness possible. This surface shows some steps between the flat regions. These steps are 0.33 nm, they are actually steps of graphene layers. Sometimes the upper layer is not perfectly aligned with the underlying layer, that's why Moiré pattern appears [31].

We choose graphite as substrate for molecules because its surface has exactly the structure of graphene, since graphite is just a pack of graphene layers. The procedure for deposition is the same for gold, but the result is different. After 1 minute

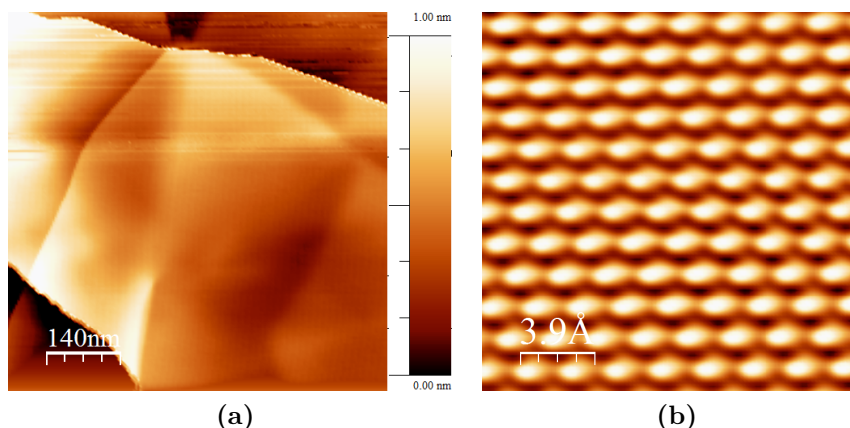


**Figure 4.4.:** (a) Large area STM image with two steps: one on top side and one on the bottom left side. (b) STM atomic resolution image of HCP lattice.

deposition no molecule is visible. Our first idea is that these molecules on graphite are so mobile that the tip moves them during the scanning. Literature [21] reports that scanning probe techniques on graphite with molecules are quite tricky and that the best condition to do microscopy is in liquid condition. DBA on graphite in UHV isn't reported yet.

Only after ten more minutes deposition and two hours annealing at 200°C we find some networks, but only around the steps. Contrary to the behavior on gold, we cannot find any single molecules. The only way to scan and image these networks is by setting "gentle" parameters: standard value for bias voltage ( $\sim 1$  V) and low tunneling current ( $< 0.015$  nA), it means that the tip is farther from the surface than usual. Fig. 4.5a, b show what happens after a strong passage of the tip with standard scanning settings: the network appears completely destroyed and on top of the step (right side of Fig. 4.5b) white irregular bands are the traces of molecules displaced by tip passages. Since higher current values are forbidden, no spectroscopy is possible, so what we can do is just precisely analyzing topography features. The larger network found is shown in Fig. 4.5c. It is possible to recognize the step (red region) which divides the two levels of the graphite (yellow, the higher and blue) and the network (light blue island). The size of this network is comparable to the ones on gold, but we emphasize that on gold we can find networks also in the middle of a flat region, here only in the presence of a defect like steps which works as nucleation point. Fig. 4.5d shows a sub-molecular resolution of a network. We can easily recognize the three benzene rings of a single molecule but also a molecule which occupies the position of a pore, another proof of the instability of these molecules. The conclusion is that the interaction of DBA-OC<sub>4</sub> with Au(111) is much stronger than with HOPG.

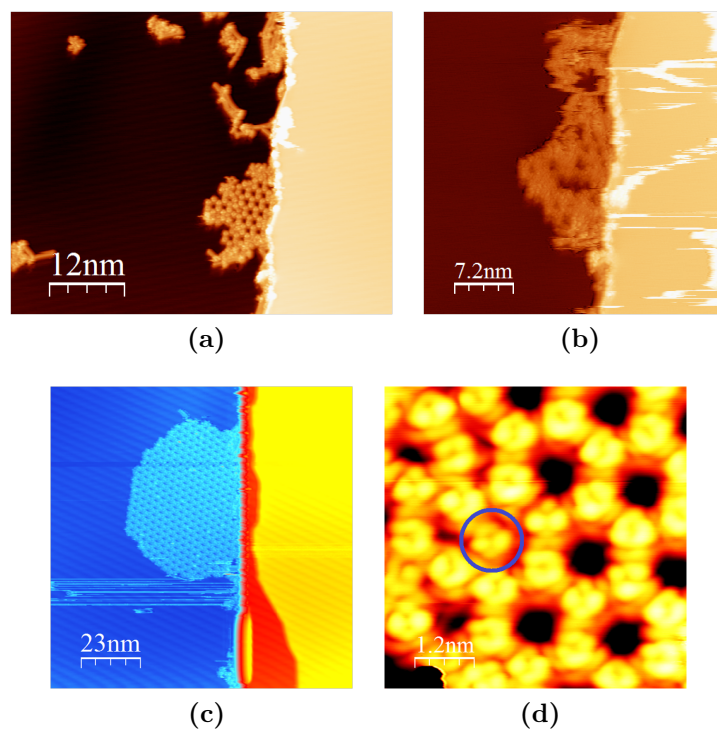


**Figure 4.5.:** DBA network close to the step (a) before and (b) after a “strong” passage of the tip. (c) 50 nm network, horizontal parallel lines are caused by the picking up of a molecule during scanning. (d) Molecular resolved networks, inside the blue circle a molecule in the wrong position in the middle of a pore.



## 5. Conclusions and Outlooks

The first goal of this thesis project was to manufacture a good graphene sample and to investigate it with scanning probe techniques. The process based on Chemical Vapor Deposition (CVD) which allows the transferring of graphene on every desired substrate was improved. Graphene on gold surfaces and graphene on silicon wafers were produced. To get atomically flat surfaces, gold was grown by Molecular Beam Epitaxy (MBE) on mica crystals. Graphene has been investigated with Atomic Force Microscope (AFM) to evaluate its quality. Our graphene was about 50% bilayer due to the CVD growth. Apart from some chemical contamination, it was homogeneous and flat enough for Ultra High Vacuum Scanning Tunneling Microscopy (STM) measurements, despite the complete *ex situ* fabrication. Large scale STM images of graphene on gold confirmed the same morphology seen with AFM. Atomic resolution scans showed the expected honeycomb lattice, but also other interesting features like grain boundaries, caused by the growth process, and double Moirè pattern which is the proof of the presence of two layers of graphene. Scanning Tunneling Spectroscopy (STS) confirmed the theoretical V shaped Local Density Of States (LDOS), but with a little *n*-doped effect likely caused by charge transfer with the gold. The other goal of the thesis was to investigate self-assembled molecules on graphene. The molecules we used were dehydrobenzo[12]annulene (DBA) provided by the University of Tokyo. Molecules deposited on gold behaved very well: it was possible investigating both single molecules and networks. The spectroscopy revealed interesting electron confinement in the pores of the networks. Molecules on graphite were found to exhibit a very different behavior because they were more mobile than on gold, therefore they were moved by STM tip during scanning. Accordingly, single molecules imaging and spectroscopy was impossible. The outlook is to deposit DBA or other molecules on graphene to test their behavior on it, particularly if they can open a band gap in its LDOS.





# Acknowledgments

I would like to thank my parents which supported my studies for all these years. All my professors, with a special thank to my supervisor Prof. Giampaolo Mistura and to Prof. Michela Fantin, a life mentor. The SPM group of KU Leuven particularly Professor Chris Van Haesendonck, dr. Koen Schouteden, Tsveta Ivanova and dr. Chundong Wang. Thanks also to you, M.M.



# A. Tight-binding method for graphene

Using tight-binding method [48] we can obtain dispersion relation of  $\pi$  bands in graphene, which are the basis to understand its interesting behavior. The molecular orbital (MO) may be written in terms of a linear combination of atomic orbitals and using the linear variational method. Graphene is a material made of carbon with  $sp^2$ -hybridization, which means that one  $p_z$ -orbital (a  $\pi$ -state) is completely decoupled from the three bonding orbitals. This means that most (low-energy) electronic properties can be determined solely by the loosely bound  $\pi$ -states. The MO  $|\Psi(\mathbf{r})\rangle$  may therefore be written as

$$|\Psi(\mathbf{r})\rangle = \sum_{j=1}^{N_a} c_{\mathbf{k}j} |\phi(\mathbf{r} - \mathbf{R}_j)\rangle \quad (\text{A.1})$$

where  $N_a$  is the number of atoms,  $\mathbf{R}_j$  is the position of the  $j$ 'th atom,  $|\phi(\mathbf{r})\rangle$  is the wavefunction of a single  $p_z$ -orbital and  $c_{\mathbf{k}j}$  are constants. Using the notation from Fig. 1.3 it is seen that we have two sublattices. One containing the A atoms and one containing the B atoms. We simplify the notation by introducing  $|\pi_{\mathbf{R}_j}^A\rangle \equiv |\phi(\mathbf{r} - \mathbf{R}_j^A)\rangle$  and  $|\pi_{\mathbf{R}_j}^B\rangle \equiv |\phi(\mathbf{r} - \mathbf{R}_j^B)\rangle$  and write

$$|\alpha\rangle = \sum_{j=1}^N c_{\mathbf{k}j} |\pi_{\mathbf{R}_j}^A\rangle, \quad |\beta\rangle = \sum_{j=1}^N c_{\mathbf{k}j} |\pi_{\mathbf{R}_j}^B\rangle \quad (\text{A.2})$$

where  $N$  is the number of unit cells,  $|\alpha\rangle$  is the MO of the A sublattice and  $|\beta\rangle$  is the MO of the B sublattice.  $|\alpha\rangle$  and  $|\beta\rangle$  will obey the Bloch condition if

$$c_{\mathbf{k}j} = \frac{1}{\sqrt{N}} e^{i\mathbf{k} \cdot \mathbf{R}_j} \quad (\text{A.3})$$

where  $\frac{1}{\sqrt{N}}$  ensures normalized MO wave functions. The expressions for  $|\alpha\rangle$  and  $|\beta\rangle$  therefore become

$$|\alpha\rangle = \sum_{j=1}^N \frac{1}{\sqrt{N}} e^{i\mathbf{k} \cdot \mathbf{R}_j} |\pi_{\mathbf{R}_j}^A\rangle \quad (\text{A.4})$$

$$|\beta\rangle = \sum_{j=1}^N \frac{1}{\sqrt{N}} e^{i\mathbf{k} \cdot \mathbf{R}_j} |\pi_{\mathbf{R}_j}^B\rangle \quad (\text{A.5})$$

The Hamiltonian and overlap matrices from the linear variational method may now be constructed from these wave functions. If only nearest neighbor interaction is assumed, the Hamiltonian matrix becomes

$$\mathbf{H} = \begin{pmatrix} H_{11} & H_{12} \\ H_{21} & H_{22} \end{pmatrix} = \begin{pmatrix} \langle \alpha | \hat{H} | \alpha \rangle & \langle \alpha | \hat{H} | \beta \rangle \\ \langle \beta | \hat{H} | \alpha \rangle & \langle \beta | \hat{H} | \beta \rangle \end{pmatrix} \quad (\text{A.6})$$

where the diagonal terms equal the on-site energy  $\epsilon_{2p}$  and the off-diagonal terms may be evaluated as

$$\langle \alpha | \hat{H} | \beta \rangle = \frac{1}{N} \sum_{i=1}^N \sum_{j=1}^N \frac{1}{\sqrt{N}} e^{i\mathbf{k} \cdot (\mathbf{R}_j - \mathbf{R}_i)} \langle \pi_{\mathbf{R}_j}^A | \hat{H} | \pi_{\mathbf{R}_j}^B \rangle \quad (\text{A.7})$$

This expression may be simplified by noting that only the difference between  $\mathbf{R}_j$  and  $\mathbf{R}_i$  enters the expression. This means that the double sum will give the same value  $N$  times. We may therefore reduce the expression to only containing one sum by taking  $\mathbf{R}_0$  as a reference for the  $i$  sum and multiplying by  $N$

$$\langle \alpha | \hat{H} | \beta \rangle = \frac{1}{N} \sum_{j=1}^N \frac{1}{\sqrt{N}} e^{i\mathbf{k} \cdot (\mathbf{R}_j - \mathbf{R}_0)} \langle \pi_{\mathbf{R}_j}^A | \hat{H} | \pi_{\mathbf{R}_j}^B \rangle \quad (\text{A.8})$$

The off-diagonal terms of the Hamiltonian are simplified by defining the transfer integral as

$$\gamma \equiv - \langle \pi_i^A | \hat{H} | \pi_j^B \rangle \quad (\text{A.9})$$

where  $|\pi_i^A\rangle$  and  $|\pi_j^B\rangle$  are nearest neighbors, such that

$$\langle \alpha | \hat{H} | \beta \rangle = -\gamma h(\mathbf{k}) \quad (\text{A.10})$$

where

$$h(\mathbf{k}) = \sum_{j=1}^N e^{i\mathbf{k} \cdot (\mathbf{R}_j - \mathbf{R}_0)} \quad (\text{A.11})$$

As the Hamiltonian operator  $\hat{H}$  is Hermitian, the Hamiltonian matrix becomes

$$\mathbf{H} = \begin{pmatrix} \epsilon_{2p} & -\gamma h(\mathbf{k}) \\ -\gamma h(\mathbf{k})^* & \epsilon_{2p} \end{pmatrix} \quad (\text{A.12})$$

The overlap matrix is given by

$$\mathbf{S} = \begin{pmatrix} \langle \alpha | \alpha \rangle & \langle \alpha | \beta \rangle \\ \langle \beta | \alpha \rangle & \langle \beta | \beta \rangle \end{pmatrix} \quad (\text{A.13})$$

The diagonal terms equal unity as the wave functions are normalized. The off-diagonal elements are calculated in a similar manner as the Hamiltonian matrix

$$\langle \alpha | \beta \rangle = sh(\mathbf{k}) \quad (\text{A.14})$$

where the overlap integral  $s$  is given by

$$s = \langle \pi_i^A | \pi_j^B \rangle \quad (\text{A.15})$$

The overlap matrix may then be written as

$$\mathbf{S} = \begin{pmatrix} 1 & sh(\mathbf{k}) \\ sh(\mathbf{k})^* & 1 \end{pmatrix} \quad (\text{A.16})$$

Now solve the Schroedinger equation  $\mathbf{H} |\Psi(\mathbf{r})\rangle = E \mathbf{S} |\Psi(\mathbf{r})\rangle$  means solve  $\det(\mathbf{H} - E\mathbf{S}) = 0$ , which gives

$$E(\mathbf{k}) = \frac{\epsilon_{2p} \mp \gamma |h(\mathbf{k})|}{1 \pm s |h(\mathbf{k})|} = \frac{\epsilon_{2p} \mp \gamma \sqrt{f(\mathbf{k})}}{1 \pm s \sqrt{f(\mathbf{k})}}$$

with  $f(\mathbf{k}) \equiv |h(\mathbf{k})|^2$  calculated from A.11

$$f(\mathbf{k}) \equiv |h(\mathbf{k})|^2 = 1 + 4 \cos^2 \left( k_y \frac{a}{2} \right) + 4 \cos \left( k_y \frac{a}{2} \right) \cos \left( k_x \frac{a\sqrt{3}}{2} \right). \quad (\text{A.17})$$

*Some passages are taken from Soren J. Brun's work, tanks to his permission.*



# Bibliography

- [1] Ariel, V., and A. Natan (2013), Electron effective mass in graphene, in *Electromagnetics in Advanced Applications (ICEAA), 2013 International Conference on*, pp. 696–698, IEEE.
- [2] Barth, C., and M. Reichling (2001), Imaging the atomic arrangements on the hightemperature reconstructed a-al<sub>2</sub>o<sub>3</sub>(0001) surface, *Nature*, 414, 54–57.
- [3] Binnig, G., and H. Rohrer (1983), Scanning tunneling microscopy, *Surface Science*, 126, 236–244.
- [4] Binnig, G., C. Quate, and C. Gerber (1986), Atomic force microscopy, *Phys. Rev. Lett.*, 56, 930–933.
- [5] Binnig, G., H. Rohrer, C. Gerber, and E. Weibel (1993), Surface studies by scanning tunneling microscopy, in *Scanning Tunneling Microscopy*, pp. 31–35, Springer.
- [6] Bistritzer, R., and A. H. MacDonald (2011), Moire bands in twisted double-layer graphene, *Proceedings of the National Academy of Sciences*, 108(30), 12,233–12,237.
- [7] Blake, P., E. Hill, A. Castro Neto, K. Novoselov, D. Jiang, R. Yang, T. Booth, and A. Geim (2007), Making graphene visible, *Applied Physics Letters*, 91(6), 063,124–063,124.
- [8] Cao, P., J. O. Varghese, K. Xu, and J. R. Heath (2012), Visualizing local doping effects of individual water clusters on gold (111)-supported graphene, *Nano letters*, 12(3), 1459–1463.
- [9] Castro, E. V., K. Novoselov, S. Morozov, N. Peres, J. L. Dos Santos, J. Nilsson, F. Guinea, A. Geim, and A. C. Neto (2007), Biased bilayer graphene: semiconductor with a gap tunable by the electric field effect, *Physical Review Letters*, 99(21), 216,802.
- [10] Choi, W., I. Lahiri, R. Seelaboyina, and Y. S. Kang (2010), Synthesis of graphene and its applications: a review, *Critical Reviews in Solid State and Materials Sciences*, 35(1), 52–71.
- [11] Coletti, C., C. Riedl, D. S. Lee, B. Krauss, L. Patthey, K. von Klitzing, J. H. Smet, and U. Starke (2010), Charge neutrality and band-gap tuning of epitaxial graphene on sic by molecular doping, *Physical Review B*, 81(23), 235,401.

- 
- [12] Dong, X., D. Fu, W. Fang, Y. Shi, P. Chen, and L.-J. Li (2009), Doping single-layer graphene with aromatic molecules, *Small*, 5(12), 1422–1426.
- [13] Emtsev, K. V., et al. (2009), Towards wafer-size graphene layers by atmospheric pressure graphitization of silicon carbide, *Nature materials*, 8(3), 203–207.
- [14] Ferreira, E. M., M. V. Moutinho, F. Stavale, M. Lucchese, R. B. Capaz, C. Achete, and A. Jorio (2010), Evolution of the raman spectra from single-, few-, and many-layer graphene with increasing disorder, *Physical Review B*, 82(12), 125,429.
- [15] Freitag, M. (2011), Graphene: Trilayers unravelled, *Nature Physics*, 7(8), 596–597.
- [16] Gao, W., and A. Kahn (2003), Controlled p doping of the hole-transport molecular material n, *Journal of Applied Physics*, 94(1), 359–366.
- [17] Geim, A. (2012), Graphene prehistory, *Physica Scripta*, 2012(T146), 014,003.
- [18] Giessibl, F. (1995), Atomic-resolution of the silicon (111)-(7x7) surface by atomic force microscopy, *Science*, 267, 68–71.
- [19] Giessibl, F., S. Hembacher, H. Bielefeldt, and J. Mannhart (2000), Subatomic features on the silicon (111)-(7x7) surface observed by atomic force microscopy, *Science*, 289, 422–425.
- [20] Graphenea (2014), Cvd graphene - creating graphene via chemical vapour deposition.
- [21] Griessl, S., M. Lackinger, M. Edelwirth, M. Hietschold, and W. M. Heckl (2002), Self-assembled two-dimensional molecular host-guest architectures from trimesic acid, *Single Molecules*, 3(1), 25–31.
- [22] Guo, B., L. Fang, B. Zhang, and J. R. Gong (2011), Graphene doping: a review, *Insciencas J.*, 1(2), 80–89.
- [23] Güttinger, J., F. Molitor, C. Stampfer, S. Schnez, A. Jacobsen, S. Dröscher, T. Ihn, and K. Ensslin (2012), Transport through graphene quantum dots, *Reports on Progress in Physics*, 75(12), 126,502.
- [24] Hasegawa, Y., and P. Avouris (1993), Direct observation of standing wave formation at surface steps using scanning tunneling spectroscopy, *Physical review letters*, 71(7), 1071.
- [25] Heyraud, J., and J. Metois (1980), Anomalous 13 422 diffraction spots from (111) flat gold crystallites:(111) surface reconstruction and moire fringes between the surface and the bulk, *Surface Science*, 100(3), 519–528.
- [26] Hong, G., Q.-H. Wu, J. Ren, C. Wang, W. Zhang, and S.-T. Lee (2013), Recent progress in organic molecule/graphene interfaces, *Nano Today*, 8(4), 388–402.
- [27] Horcas, I., R. Fernández, J. M. G. Rodr'iguez, J. Colchero, J. G. Herrero, and A. M. Baro (2007), WSXM: A software for scanning probe microscopy and



- a tool for nanotechnology, *Review of Scientific Instruments*, 78(1), 013,705+, doi:10.1063/1.2432410.
- [28] Kim, J.-H., K. Tahara, J. Jung, S. De Feyter, Y. Tobe, Y. Kim, and M. Kawai (2012), Ordering of molecules with pi-conjugated triangular core by switching hydrogen bonding and van der waals interactions, *The Journal of Physical Chemistry C*, 116(32), 17,082–17,088.
- [29] Kim, J.-H., J. Jung, K. Tahara, Y. Tobe, Y. Kim, and M. Kawai (2014), Direct observation of adsorption geometry for the van der waals adsorption of a single pi-conjugated hydrocarbon molecule on au (111), *The Journal of chemical physics*, 140(7), 074,709.
- [30] Kittel, C., and P. McEuen (1976), *Introduction to solid state physics*, vol. 8, Wiley New York.
- [31] Li, G., A. Luican, and E. Y. Andrei (2009), Scanning tunneling spectroscopy of graphene on graphite, *Physical review letters*, 102(17), 176,804.
- [32] Li, X., et al. (2009), Large-area synthesis of high-quality and uniform graphene films on copper foils, *Science*, 324(5932), 1312–1314.
- [33] Lobo-Checa, J., M. Matena, K. Muller, J. H. Dil, F. Meier, L. H. Gade, T. A. Jung, and M. Stohr (2009), Band formation from coupled quantum dots formed by a nanoporous network on a copper surface, *Science*, 325(5938), 300–303.
- [34] Lu, Y., B. Goldsmith, D. R. Strachan, J. H. Lim, Z. Luo, and A. Johnson (2010), High-on/off-ratio graphene nanoconstriction field-effect transistor, *Small*, 6(23), 2748–2754.
- [35] Mattevi, C., H. Kim, and M. Chhowalla (2011), A review of chemical vapour deposition of graphene on copper, *Journal of Materials Chemistry*, 21(10), 3324–3334.
- [36] Melle, H., and E. Menzel (1978), Superstructures on spherical gold crystals, *Zeitschrift Naturforschung Teil A*, 33, 282.
- [37] Miller, D. L., K. D. Kubista, G. M. Rutter, M. Ruan, W. A. de Heer, P. N. First, and J. A. Stroscio (2010), Structural analysis of multilayer graphene via atomic moire interferometry, *Physical Review B*, 81(12), 125,427.
- [38] Moore, G. E., et al. (1965), Cramming more components onto integrated circuits.
- [39] Neto, A. C., F. Guinea, N. Peres, K. S. Novoselov, and A. K. Geim (2009), The electronic properties of graphene, *Reviews of modern physics*, 81(1), 109.
- [40] Novoselov, K. S., V. Fal, L. Colombo, P. Gellert, M. Schwab, K. Kim, et al. (2012), A roadmap for graphene, *Nature*, 490(7419), 192–200.
- [41] Pembroke, E., G. Ruan, A. Sinitskii, D. A. Corley, Z. Yan, Z. Sun, and J. M. Tour (2013), Effect of anchor and functional groups in functionalized graphene devices, *Nano Research*, 6(2), 138–148.

- 
- [42] Petersen, L., et al. (1998), Direct imaging of the two-dimensional fermi contour: Fourier-transform stm, *Physical Review B*, 57(12), R6858.
  - [43] Rudolph, R., C. Pettenkofer, A. A. Bostwick, J. A. Adams, F. Ohuchi, M. A. Olmstead, B. Jaeckel, A. Klein, and W. Jaegermann (2005), Electronic structure of the si (1 1 1): Gase van der waals-like surface termination, *New Journal of Physics*, 7(1), 108.
  - [44] Schwierz, F. (2010), Graphene transistors, *Nature nanotechnology*, 5(7), 487–496.
  - [45] Seo, Y., and W. Jhe (2008), Atomic force microscopy and spectroscopy, *Rep. Prog. Phys.*, 71.
  - [46] Shimizu, T. K., J. Jung, T. Otani, Y.-K. Han, M. Kawai, and Y. Kim (2012), Two-dimensional superstructure formation of fluorinated fullerene on au (111): A scanning tunneling microscopy study, *ACS nano*, 6(3), 2679–2685.
  - [47] Swart, I., L. Gross, and P. Liljeroth (2011), Single-molecule chemistry and physics explored by low-temperature scanning probe microscopy, *Chemical Communications*, 47(32), 9011–9023.
  - [48] Wallace, P. R. (1947), The band theory of graphite, *Phys. Rev.*, 71, 622–634, doi:10.1103/PhysRev.71.622.
  - [49] Wofford, J. M., et al. (2012), Extraordinary epitaxial alignment of graphene islands on au (111), *New Journal of Physics*, 14(5), 053,008.
  - [50] Zhang, Y., T.-T. Tang, C. Girit, Z. Hao, M. C. Martin, A. Zettl, M. F. Crommie, Y. R. Shen, and F. Wang (2009), Direct observation of a widely tunable bandgap in bilayer graphene, *Nature*, 459(7248), 820–823.
  - [51] Zhu, W., T. Low, V. Perebeinos, A. A. Bol, Y. Zhu, H. Yan, J. Tersoff, and P. Avouris (2012), Structure and electronic transport in graphene wrinkles, *Nano letters*, 12(7), 3431–3436.